DOE/VTO – DE-EE0008870:

Final Report

Reporting Period: 09/19/2019-12/31/2022
Date of Submission of Report: March 31, 2023

Federal Agency/ Organization Element:	DOE/EERE/ Vehicle Technology Office (VTO)
Award Number:	DE-EE0008870
Project Title:	Amorphous Metal Ribbon (AMR) and Metal Amorphous Nanocomposite (MANC) Materials Enabled High Power Density Vehicle Motor Applications.
Project Period:	Start Date: 09/19/2019 – End Date: 09/18/2022
Recipient Organization:	Carnegie Mellon University 5000 Forbes Ave Pittsburgh PA 15213-3815
DUNS Number:	052184116
Principal Investigator	Michael McHenry, 412-268-2703, mm7g@andrew.cmu.edu
Business Contact:	Anthony Talotta, 412-268-5765, atalotta@andrew.cmu.edu
Partners:	North Carolina State University Metglas
DOE Technology Manager:	Susan Rogers, 202-975-2071, Susan.rogers@ee.doe.gov
DOE Project Officer:	Benjamin May, 304-282-3256, Benjamin.May@netl.doe.gov
DOE Contract Specialist:	Amanda Lopez, 304-285-4220, Amanda.lopez@netl.doe.gov
DOE Contracting Officer:	Susan Miltenberger, 304-285-4083, Susan.Miltenberger@netl.doe.gov
Submitting Official:	Michael E. McHenry, Professor, 412-268-2703, mm7g@andrew.cmu.edu

---

VTO Electrification 2023 Final Report: DOE/EERE/ Vehicle Technology Office (VTO) DE-EE008870

Amorphous Metal Ribbon (AMR) and Metal Amorphous Nanocomposite (MANC) Materials Enabled High Power Density Vehicle Motor Applications. Carnegie Mellon Univ.

Table of Contents

I. Project Introduction

A collaborative team from ***Carnegie Mellon Univ. (CMU), North Carolina State Univ. (NCSU)*** and ***Metglas, South Carolina*** have studied new high speed motors (HSMs) with high-power density for traction motor applications. These are enabled by hybrid designs, including Flux Switching with Permanent Magnets (FSWPM) motors, exploiting permanent magnets without heavy rare earths (RE-lean) and high induction/high resistivity soft magnetic materials that allow for high switching frequencies needed to increase power densities.

Team members include **Michael E. McHenry**, Prof. Materials Science & Eng., CMU, with > 30 years experience in magnetic materials development; **Subashish Bhattacharya**, Prof. Electrical Eng. and Freedom Center Director at NCSU with > 30 years experience in development of power electronic components and systems and **Eric Theisen**, Director of Research at Metglas, the only US located supplier of AMR and MANC materials. The team offers novel axial motor architectures exploiting soft magnetic materials (SMMs) that switch with low loss at high frequencies and heavy rare earth free permanent magnets that address materials criticality issues, supply chain risks, and high costs for traction motors.

Axial-flux permanent magnet motors (APFM), offer efficiency improvements reducing rotor losses and also significantly higher power density. Axial-flux construction requires less core material, high torque-to-weight ratio. Since AFPM machines have thin magnets, they are smaller than radial flux motors making them attractive in space-limited applications. Noise and vibration are less and planar air gaps are easily adjusted. Flexibility in air-gap direction allows many topologies.

II. Objectives

The project objective is to achieve 8-fold increase in power density for an axial motor designed to showcase Amorphous Metal Ribbon (AMR) and Metal Amorphous Nanocomposites (MANCs). Motors are enabled by hybrid designs exploiting rare earth lean permanent magnets and high induction/high resistivity soft MANC allowing high switching frequencies needed to increase power densities.

III. Approach

Technical components, completed in budget periods, BP1 and BP2, are summarized:

Budget Period 1: Benchmark AMRs and MANC Alloys for HSM Design: AMR materials will be benchmarked, in a Finite Element Analysis (FEA) model. Alloys will be cast at commercial scale and properties relevant to 5 kHz magnetic core losses and audible magnetostrictive losses will be measured and compiled. Sample ribbons will be provided to the DOE. A FEA model of a Traction High Speed Motor (HSM) will be designed and performance evaluated.

Budget Period 2: Properties Optimization, Component Fabrication and Alloy Studies.: Properties of AMR materials will be optimized and benchmarked. Rotors and dual stators will be produced for testing and loss validation in the Flux Switching with Permanent Magnet (FSWPM) motor. Magnetic switching frequencies and mechanical properties will be evaluated. The measured properties will be incorporated into a FEA model of a Traction HSM and used to finalize the design. This design will be used to benchmark new materials.

IV. Budget Period 1 Task Completion Chronology and Milestone Completion Table.

Budget Period 1: Task Completion Chronology

Task 0.0 – Project Management Plan: was submitted and approved. **Complete.**

Task 0.1- Kick-Off Meeting: was held at CMU. 11/22/2020. **Complete.**

Budget Period 1, 1st Quarter Tasks:

Task 1.1 – Staff and train project personnel:

Subtask 1.1.1 – Staff was allocated staff for the Project as summarized (App. 1). **Complete**

Subtask 1.1.2 – CMU continued licenses for Comsol Multiphysics FEA Software and maintained supplies of raw materials & casting expendables for subsequent Tasks. **Complete**

Subtask 1.1.3 – CMU identified suppliers for permanent magnets in Q1 Report. **Complete**.

Budget Period 1, 2nd Quarter Tasks:

Task 1.2 – FEM Motor Modeling, Alloy Development:

Subtask 1.2.1 – CMU benchmarked Al&Cu wire conductors and permanent magnets in FSWPM HSM Design. **Complete.**

Subtask 1.2.2 – Metglas FeCo-based AMR were benchmarked in FSWPM HSM Design. AMR was produced at scale. Motor design and parameters were reported. **Complete**

Subtask 1.2.3 – FeNi-based MANC alloys were cast at scale. A new FeNi-based MANC alloy exhibited an induction >1.5 T. **Complete**

Subtask 1.2.4 – Quadrant was identified as a source of permanent magnets. Permanent magnets were supplied by Quadrant**. Complete**

Budget Period 1, 3rd Quarter Tasks:

Task 1.3– Begin FeCo AMR Casting Trials, Measure Properties:

Subtask 1.3.1 – CMU identified FEM topology and 2-d grids for HSM with > 5 kHz. **Complete.**

Subtask 1.3.2 –Metglas cast FeCo-based AMR in 2" wide ribbon for evaluation. CMU received 40 mm wide ribbon from Metglas. Metglas provided properties data**.** CMU measured high frequency losses frequencies 07/27/2020. **Complete.**

Subtask 1.3.3 – We measured Magnetostriction in Metglas FeCo- and FeNi-based AMRs. Magnetostriction on 40 mm wide AMR was reported in a quarterly reports**.** K. Schneider constructed in-house strain guage methods for magnetostriction measurement. **Complete.**

Subtask 1.3.4 – CMU measured M(T), Bs, Tc, Crystallization temperatures and AC Losses. Bs, Tc, to corroborate Metglas reported numbers. **Complete**.

Budget Period 1, 4th Quarter Tasks:

Task 1.4 – Screen Properties of MANC Alloys:

Subtask 1.4.1 – Identify and Cast 2nd Generation FeNi MANC Alloy at Scale. **Complete**.

Subtask 1.4.2 – We measured Bs, Tc, Crystallization T and AC Losses for MANCs. **Complete**.

Subtask 1.4.3 – We measured Magnetostriction in FeNi-based MANC Alloys. **Complete**.

Subtask 1.4.4 – We initiated thinning studies of FeNi MANC Alloys. **Complete**.

Budget Period 1, 5th Quarter Tasks:

Task 1.5– We evaluated materials in FEA Motor Design:

Subtask 1.5.1 – We benchmarked conductors in Traction HSM Design. **Complete**.

Subtask 1.5.2 – Benchmark Metglas FeCo-based AMR in Traction HSM Design. **Complete**.

Subtask 1.5.3 – Benchmark Metglas FeNi-based MANC in Traction HSM Design. **Complete**.

Subtask 1.5.4 – Report Power Density Improvement with AMRs and MANCs. **Complete**

BP1 Milestone Completion Chronology

Milestones 1-4 were completed as summarized in Table 1.

Milestone 1: A motor design was reported to meet **Milestone 1**. **Completed** 06/22/2020.

Milestone 2: Wide cast AMR and MANC ribbon evaluation to 5 kHz was **Completed** 12/15/20.

Milestone 3: Power Density Improvement Evaluations were **Completed** 04/14/21.

Milestone 4: FEA assessment of preliminary technology design verified an 8x increase in power to be achievable at 34 kW power **Completed** 06/15/21.

Milestone	Description	Planned Competion Date	Actual Completion Date
Budget Period 1			
Design Traction Motor	Benchmark materials. Report FSWPM Motor Power Losses	6/15/20	6/22/20
AMR Loss at 5kHz Evaluation Complete	Compare wide cast AMR and MANC Ribbon evaluation at 5 kHz	12/15/20	12/15/20
Evaluate Materials in Traction Motor Design Ide	Complete Power Density Improvement Evaluation with AMRs and MANCs.	4/15/21	4/14/21
Preliminary Design Validated to Achieve Performance Measures	FEA assessment of preliminary technology design has been completed, verifying an 8x increase in power density to be achievable.	6/15/21	6/15/21

Table 1: BP1 Milestone Schedule (including NCE):

V. BP1 Accomplishments: In BP1, the team staffed the project and had a kickoff meeting. BP1 Tasks had the following accomplishments, listed by quarter:

BP1 Q1

Task 1.1 – Staff and train project personnel:

Subtask 1.1.1 – Allocate staff for the Project: We staffed the project as (**App. 1**). Team members include **Prof. M. E. McHenry**, Mat. Sci. & Eng., CMU and **Prof. M. De Boer,** Mechanical Eng., CMU; **Prof. S. Bhattacharya**, Elec. Eng. & Freedom Center Director, NCSU, and **E. Theisen**, Research, Metglas, US supplier of AMR & MANC materials. CMU Senior Scientist, **S. Simizu**, supervised motor design. CMU visiting scientist, **G. Bellesis**, investigated magnetostriction leaving for a position with Phillips in 2020. **Y. Krimer** (Carpenter funded) investigated new FeNi-based AMRs and glass forming ability for HSMs. He alloy reported inductions > 1.5 T and defended a 2021 CMU MSE Ph.d thesis. **J. Egbu** (GEM fellow) investigated FeNi-based MANC oxidation and epoxy wetting. He will defend his MSE thesis in April, 2023. **K. Schneider** (CMU Mech. Eng.) investigated magnetostriction and mechanical properties for HSMs. He worked with S. Simizu to benchmark materials in a 34-kW motor design. **W. Harrison** (CMU Mech. Eng.) investigated mechanical properties and moved to another project.

Subtask 1.1.2 – CMU maintained software licenses, components, expendables for alloy studies. Comsol Multiphysics FEA software licenses for electromagnetic, thermal and mechanical properties were obtained and graduate students trained on these modules.

Subtask 1.1.3 – George Bellesis evaluated PM suppliers and identified **Quadrant** to supply sector magnets required for our FSWPM HSM **Complete** 11/20/2019.

BP1 Q2

Task 1.2 – Begin FEM Motor Modeling, Alloy Development:

Subtask 1.2.1 – Benchmark conductors, REPMs in FSWPM HSM Design **(Complete)**. Al and Cu motor coil conductors were investigated. Cu has lower resistivity but higher density. In an AMO constructed 2.5 kW FSWPM motor prototype, Joule heating power loss was 34 W at maximum current for Cu coils

with assumed 50 % filling. Power loss increases to 52 watts with Al. Coil mass is reduced from 0.52 kg to 0.16 kg if Cu is replaced by Al, a ~7 % of saving of total conductor mass.

Our AMO 2.5 kW FSWPM motor considered a low remanence magnet, addressing RE criticality. To achieve higher power density we adopted NdFeB permanent magnets supplied by **Quadrant.** We addressed RE criticality by limiting the heavy RE, Dy, reducing REPM cost. The NdFeB magnet size is much smaller than hard ferrites used in the 2.5 kW motor, because of much higher energy product. Reduced requirements for PM coercivity allowed use of Dy-free PMs. We received NdFeB magnets with coercivity requirements met with < 1.5% Dy.

Subtask 1.2.2 – Benchmark Metglas FeCo-based AMR in prior FSWPM HSM Design: We considered several SMMs for design of the FSWPM motor. Silicon (3%) steel is widely used for HSM motors but its high-power loss at high *f* precludes use for switching *f* > 1 kHz. MANC SMMs are attractive for low power loss at high-f. Fe-Ni-based MANCs show very low power loss above 1 kHz; its operating f may be extended to ~5 kHz. Its maximum flux density (1.3 T) limited the high-power density design. We thus also considered FeCo-based AMRs produced commercially by Metglas (**App. 2**).

Metglas Alloy 2605CO (**App. 3**) has high as-cast (1.66 T) and annealed induction (1.78 T) of interest for high power density HSMs. A flux density of an optimally annealed product may reach 1.8 T, but with relatively high power loss. We also identified Fe-Ni-based MANCs with higher, 1.53 T, flux density by increasing Fe-Ni content from 80 % to 85 %. This provides a design option if power losses are optimized in subsequent work. A > 20 kW axial motor design was compared with a 2.5 kW FSWPM motor (**App. 4)**. An 8-fold power density increase is achieved by combining increased speed (1.5x), MANC induction (> 2x), permanent magnet remanence (2.5x), conductor fill factor (1.3x), radius (1.5x) and # of salient poles (1.5x) while maintaining a coil to pole ratio at 6:7.

Subtask 1.2.3 – Begin Casting New FeNi-based MANC alloys: **App. 5** summarizes synthesis, structure, properties & performance of FeNi-based MANCs investigated for increased induction. A flux density of 1.53 T was established in one of the MANCs, but its coercivity was high. Future casting developments may improve as-cast coercivity.

Subtask 1.2.4 - Permanent magnet sourcing inquiries for a FSWPM 20 kW motor led to the choice of **Quadrant** to supply the REPMs. Quadrant was able to meet permanent magnet requirements with N38 grade NdFeB magnets with Dy content of 0~1.5 % (not necessarily 0 due to raw materials consideration). PM dimensions were chosen for our high power motor design. 108 magnets were supplied by Quadrant, to demonstrate manufacturability and evaluate magnet quality.

BP1 Q3

Task 1.3– Begin FeCo AMR Casting Trials, Measure Properties:

Subtask 1.3.1 – We identified FEM topology/2-d grids for > 5 kHz switching. **Complete**. We presented a design to increase power density of the FSWPM motor by 8x from 0.45 to 4 kW/kg while increasing rated power from 2.5 to 34 kW (**App. 4**). Mechanical speed was limited to 6 krpm (100 Hz) and electrical speed increased from 1.4 to 2.1 kHz. A maximum soft magnet flux density of ~1.54 T was assumed. The design requires NdFeB magnets with 1.2 T remanence and modest coercivity. In FEA validation, iron loss was calculated using a Steinmetz equation. f and f_0 are frequency & reference f. B & B_0 are peak flux density & reference B:

$$\sum_i a_i \left(\frac{f}{f_0}\right)^{\alpha_i} (B/B_0)^{\beta_i}$$

The equation sums hysteretic, eddy current, and anomalous losses determined for NiFe-MANC strip.

For ease of implementation, peak flux density was replaced by its instantaneous value to give an estimate (flux density is widely spatially distributed and loss values are dominated by peak values). Stator power loss was evaluated for a full electrical rotation. Calculated over the entire stator, the

loss is nearly constant. Calculated for a segment (1/6 of the total) of the stator, it shows significant variation. We determined it to be more accurate to use the segment peak value instead of the entire stator value. Losses were subsequently calculated by this method. A complication for rotor loss calculations is that for a rotor with 14 teeth, the flux pattern repeats every 1/14th of turn mechanical rotation as viewed at the stator. Observed from the rotor's frame, it must make an additional; 1/14th turn to return to the original state because the PM polarities alternate. The magnetic f experienced by the rotor is half of the drive frequency. This is favorable to control rotor iron loss.

Subtask 1.3.2 – Cast Metglas FeCo-based AMR in 2"-wide ribbon for evaluation: We received 40 mm wide ribbon from Metglas sufficient for properties measurements (properties data (**App. 3 & 4). Complete.** We additionally received ~3kgs of 85mm wide as-cast AMR from Metglas.

Subtask 1.3.3 - Measure Magnetostriction in Metglas FeCo-based AMR. 40 mm wide ribbon received from Metglas has magnetostriction coefficients listed in **App. 3. Complete.**

Subtask 1.3.4 - Measure M(T), Bs, Tc, Crystallization T's and AC Losses in Metglas FeCo-based AMR. Bs, Tc, Crystallization T's and AC Losses (400 Hz) are reported (**App. 3 & 4).** Metglas production core AC (400 Hz) loss measurements were verified at CMU with testing of 5 kHz core losses. **Complete.**

BP1 Q4

Task 1.4 – Screen Properties of MANC Alloys:

Subtask 1.4.1 – Identify and Cast 2nd Generation FeNi MANC Alloy at Scale: Metglas cast a 2nd generation FeNi MANC Alloy at scale. The ribbon exhibited larger curvature than prior FeNi alloys cast. Metglas explored options to reduce the curvature. **Complete.**

Subtask 1.4.2 – Measure Bs, Tc, Crystallization temperatures & AC Losses in FeNi-MANCs.

(FeNi)85%: Bs, Tc, T_{x1}, T_{x2}, and AC losses were measured on as-cast ribbon (**App. 5)** and magnetic properties of as-cast strip and core (**App. 8**). ~5 kgs of 1" wide ribbon was provided by Metglas. Ribbon & core annealing trials were performed. **Complete. (FeNi)80%:** We performed annealing studies to optimize AC losses and coercivity (**App. 5**). 15 kgs of 2" wide ribbon was provided by Metglas. Motor core fabrication steps were demonstrated. **Complete.**

Subtask 1.4.3 – Measure Magnetostriction in FeNi-based MANC Alloys. **Complete**

Metglas performed strain gauge measurement of magnetostriction coefficients in new alloys. We developed a technique to estimate magnetostriction coefficients from an approach to saturation analysis of M(H) to measure magnetostrictive stress induced anisotropy. CMU developed in-house strain gauge based magnetostriction techniques to corroborate Metglas results (**App. 6**). Magnetostriction techniques were developed in house. A perfected method to reduce magnetostrictive losses through stress relief annealing was developed and very low losses reported in FeNi-based MANCs as published as an Editor's featured article in J. Mat. Res.:

K. Byerly, Y. Krimer, Charudatta Phatak, E. Theisen, and M. E. McHenry, Magnetostrictive Loss Reduction through Stress Relief Annealing in an FeNi-based Metal Amorphous Nanocomposite. J. Mat. Res. **36,** 2843-55**,** (2021). https://doi.org/10.1557/s43578-021-00268-5

Subtask 1.4.4 – Initiate Thinning Studies by Rolling/Casting/Strain Annealing of FeNi MANC Alloys. **Complete**. Metglas planar flow cast thin ribbon directly (~12-15μm). A trade-off in casting thin thicknesses where ribbon exhibits pinholes, leads to reduced stacking factor of wound cores, We believe this is the most direct method to thin ribbon. We proved strain annealing to thin FeNi ribbon.

BP1 Q5

Task 1.5– BP1 Q5/NCE: Evaluate Materials in HSM Design.

Subtask 1.5.1 – Benchmark conductors in HSM Design. **Complete.**

Subtask 1.5.2 – Benchmark Metglas FeCo-based AMR in Traction HSM Design. **Complete,**

Subtask 1.5.3 – Benchmark Metglas FeNi-based MANC in Traction HSM Design. **Complete**

Subtask 1.5.4 – Report Power Density Improvements. Disseminate results. **Complete.** Task 1.5 results of were reported to the DOE. **App. 7** summarizes benchmarking results for **Milestone 3**. **App. 7** also presents 34 kW FSWPM HSM designs establishing **Milestone 4** completion and the Go/NoGo criterion and manufacturability demonstration. We were granted continuation into BP2 upon achieving our Go/NoGo metric.

Summary: In BP1, we modeled a flux switching with permanent magnet (FSWPM) motor meeting power metrics for the program goals.[1,2] This motor topology represents an 8x increase in power compared with a previous 2.5 kW design pursued with AMO funding.[1] The paper describing this technology: S. Simizu, et al.[2], was presented at the IEEE Energy Conversion Congress and Exposition, Vancouver Can., Oct. 10-14, 2021 and given Best Paper Award at the ECCE 2022 Conference, Detroit, MI. Our FSWPM motor designs are enabled by amorphous magnetic ribbon or metal amorphous nanocomposite[3,4] tape wound cores (TWCs) in their construction. Fe-Ni-based MANCs[5] with magnetostrictive losses reduced by 2-5 x with appropriate stress relief anneals[7] developed in the project and reported in K. Byerly, et al. [3]

At the Go/NoGo decision we proposed additional experiments to extend BP1 advancements into BP2 in ways not originally anticipated. We used residual BP1 funds to perform additional work:

(a) To understand epoxy resin wetting to the native oxides on the MANCs using sessile droplet wetting experiments; **App. 8** describes sessile drop contact angle measurement apparatus built for a liquid droplet on a sample to study wetting.
(b) To perform additional microscopy of MANC/Oxide/epoxy interfaces;
(c) To measure epoxy properties for FEA models to support BP2 Milestones.

BP 2 Task Completion Chronology and Milestone Completion Table.

Budget Period 2, Q1: Alloy Development, Fabricate FeCo-based Stators & Rotors. We demonstrated manufacturability of FeCo-based AMR motors:
Subtask 2.1.1 – Fabricate FeCo-based AMR rotor based. **Complete**
Subtask 2.1.2 – Fabricate FeCo-base AMR stators. **Complete**
Subtask 2.1.3 – Perform TEM & EDAX on MANC and FeCo AMR Alloys. **Complete**
Subtask 2.1.4 – Continue Alloy Development, Measure surface resistivity. **Complete**.
Budget Period 2, Q2: Measure Mechanical Properties: AMRs & MANCs. We measured mechanical properties of AMRs and MANCs:
Subtask 2.2.1 – Nanoindentation, Tensile Testing & Bend Tests. **Complete** (**App. 9**)
Subtask 2.2.2 –. Measure AMR/MANC densities and Properties. **Complete** (**App. 9**)
Subtask 2.2.3 – Initiate Thinning Studies of FeNi MANCs. **Complete.**
Subtask 2.2.4 – Develop FEA Mechanical Properties model of HSM rotor. **Complete**.
Budget Period 2, Q3: Test FeNi-based AMR Dual Stators and Rotors: We tested rotors and stators.
Subtask 2.3.1 – Demonstrate FeNi MANC rotor fabricability in HSM design. **Complete**.
Subtask 2.3.2 – Demonstrate FeNi AMR stator fabricability in HSM design. **Complete**.
Subtask 2.3.3 – Test FeCo-based dual stator FSWPM HSM with controller. **Complete**.
Subtask 2.3.4 – Estimate 20-40 krpm loss partitioning: FeCo-based HSM. **Complete.**
Budget Period 2, Q4: Identify Oxides on FeNi-, FeCo-base MANCs & AMR's. (App. 10). Oxides are identified (App. 10).
Subtask 2.4.1 – Identify Oxides on FeNi-, FeCo-base MANCs & AMR's. Complete.
Subtask 2.4.2 – Model Oxidation Mechanisms. Complete.
Subtask 2.4.3 – Confirm MANC/AMR Chemistries & Passivating Oxides. Complete.
Subtask. 2.4.4 – Perform TEM on thinned MANCs. Complete.
Budget Period 2, Q5 & NCE: Test FeNi-based MANC Dual Stators and Rotors. (App.11)
Subtask 2.5.1 – Tested FeNi-based dual stator FSWPM HSM with controller. Complete.
Subtask 2.5.2 –. Estimated 20-40 krpm loss partitioning: FeNi-based HSM. Complete.
Subtask 2.5.3 – FEA model for thinned FeNi-based FSWPM HSM performance. Complete.
Subtask 2.5.4 – Included losses in FEA HSM design; Benchmark against FeBSi Complete

BP2 Milestone Completion Chronology
BP2 Milestones 1-4 were completed as summarized in Table 1.
Milestone 1: We demonstrated manufacturability of FeCo-based AMR motor (**App. 7**) **Complete** 09/15/22.
Milestone 2: Mechanical properties verified HSM able rotate at 10 krpm **(App. 7**) **Complete** 03/15/22.
Milestone 3: We reported oxide properties for AMR and MANCs **Completed** 6/15/22.
Milestone 4: We reported HSM power density for each material. **Completed** 12/15/22.

Budget Period 2			
Fabricate FeCo-based Stator/Rotor.	Demonstrate FeCo-based AMR motor Manufacturability.	12/15/21	09/15/22
Evaluate Mechanical Properties of AMRs and MANCs Suitable for HSM	Use mechanical properties in FEA to verify that HSM is mechanically able to rotate at >20 krpm.	03/15/22	03/15/22
Report Oxide Properties of AMR/MANCs	Demonstrate resistance > coated laminates; bulk resistivity > 150 μΩ-cm; surface resistivity > 500 μΩ-cm.	6/15/22	6/15/22
Test AMR and MANC Dual Stators & Rotors.	Report HSM power density for each material.	12/31/22	NCE

Table 2: BP2 Milestone Schedule and Completion.

BP 2 Accomplishments In BP2 we continued work based on BP1, in the BP2 tasks:
Task 2.1 BP2 Q1: Alloy Development, Fabricability of FeCo-based Stators/Rotors: The goal of this work is to demonstrate manufacturability of FeCo-based AMR motors. This was first demonstrated in FeNi-based MANC motors to show manufacturability of waterjet rotor and stator cuts for high power FSWPM motor design **(App. 7).**
Subtask 2.1.1 – Fabricate FeCo-based AMR rotor sectors based on FSWPM design **100% Complete**. We demonstrated manufacturability on FeNi-based cores building on manufacturing steps of our AMO program. Manufacturability of a FeNi-based rotor segment was demonstrated (**App. 7**). We demonstrated motor speeds to 6 krpm (**App. 11**) and FEA models for the VTO topology to indicate power metrics can be attained at 10 krpm. After evaluating mechanical properties of FeNi-based MANCs, we concluded that establishing figures of safety (FOS) for larger diameter motors were necessary for > 6 krpm rotational speeds. In lieu of such tests, to compare loss partitioning between materials, Metglas investigated a modified HSM to allow MANC and AMR materials comparison using less complicated manufacturing steps for cutting/insulation than waterjet cut FSWPM topologies. A completed stator fabrication is described in **App. 12**. Metglas worked with a partner to construct FeCo-based AMR rotors and stators of **Sub-tasks 2.1.1 & 2.1.2**, to compare with Fe-Ni-based MANC soft magnets in a common topology (**App. 12**).
Subtask 2.1.2 – Demonstrated fabrication of FeCo-based AMR stators design. **Complete.** FSWPM stator designs were supplied to our collaborator. We demonstrated manufacturability of FeNi-based cores building on our AMO program. Manufacturability of an FeNi-based stator wedge is shown in **App. 7**. Given the FOS concerns expressed in Sub-task 2.1.1, we used a Metglas motor design to for loss-partitioning comparisons in **Subtask 2.5** (**App. 12**).
Subtask 2.1.3 – Perform TEM & EDAX on MANC & FeCo AMR Alloys. **100%** MANC TEM was performed on FeCo AMRs provided by Metglas. TEM analysis (**App. 10**) we observed:

(a) Featureless low magnification images are typical of an amorphous material.
(b) Electron diffraction patterns showed broad rings typical of amorphous materials. In addition there were 2 distinct rings indicating of local ordering.
(c) High resolution TEM (HRTEM) confirmed the existence of very small, sub-nanometer ordered clusters (embryos) typical in undercooled or frozen liquids**.**

Subtask 2.1.4 – Continued Alloy Development, Measure surface resistivity. **Complete**. CMU cast 10 new $Fe_{70-x}Ni_{30}Co_x$ and $Fe_{70}Ni_{30-x}Co_x$ alloys to measure T-dependent magnetic properties and crystallization T's. Results are submitted for publication (K. Snyder, et. al., JALCOM submitted). M(T) measurements were fit to T-dependent Brillouin functions to infer 0 K saturation induction (B_s). B_s exceeds 1.5 T for several alloys. Bulk and surface resistivity are reported in **App. 10** to eliminate any concerns of interlayer shorting in TWCs.

Task 2.2 BP2 Q2: Measure Mechanical Properties: AMRs & MANCs.
Subtask 2.2.1– Nanoindentation, Tensile & Bend Testing. (CMU). **100% Complete.** Nanoindentation and Bend tests were performed. Tensile test procedures were developed and performed for single ribbons and stacked epoxy impregnated ribbons. (**App. 9)**
Subtask 2.2.2–. Measure Densities & Properties of AMR & MANCs. (CMU). **Complete.** MANC and AMR densities and were documented (**App. 9**).
Subtask 2.2.3 – Initiate Thinning Studies of FeNi MANCs. (CMU). **Complete.** Thinning was demonstrated to result from strain annealing in BP1 (**App.9**)**.**
Subtask 2.2.4 – We developed a FEA Mechanical model of a HSM rotor and identified stress concentration points in our design (**App.9**)**. Complete.**

Task 2.3 BP2 Q3: Test FeNi-based AMR Dual Stators and Rotors. (App. 15)
Subtask 2.3.1 – Fabricate FeNi-based MANC rotor section based on FSWPM design. **100% Complete**. For a 34 kW motor we showed manufacturability of rotor sectors (**App. 7**).
Subtask 2.3.2 – Fabricate FeNi-based AMR stator sectors based on FSWPM design. **Complete.** For a 34 kW HSM we demonstrated stator sector manufacturability (**App. 7**) and assessed epoxy MANC vacuum impregnation bonding (**App. 8**).
Subtask 2.3.3 – Test FeCo-based HSM with controller (App. xx). **Complete.**
Subtask 2.3.4 – We estimated 20 krpm loss partitioning: FeCo-based HSM. **Complete. (App.7)**
Task 2.4– BP2 Q4: Identify Oxides on FeNi-, FeCo-base MANCs & AMR's. (App. 9).
Subtask 2.4.1 – Identify Oxides on FeNi-, FeCo-base MANCs & AMR's**. (App. 10). Complete.**
Subtask 2.4.2 – Model Oxidation Mechanisms. **Complete.**
Subtask 2.4.3 – Confirm MANC, AMRs & Passivating Oxide chemistries. **Complete.**
Subtask 2.4.4 – Perform TEM on thinned MANCs. **Complete.**
Task 2.5– BP2 Q5: Test FeNi-based MANC Dual Stators and Rotors. (App. 20)
Subtask 2.5.1 – Test FeNi-based HSM with controller. (Metglas, NCSU) **100% Complete**
Subtask 2.5.2 –. Estimate loss partitioning: FeNi-based HSM. (NCSU) **100% Complete**
Subtask 2.5.3 – FEA model performance in thinned FeNi-based HSM **100% Complete**
Subtask 2.5.4 – Incorporate measured losses in FEA traction HSM design. Benchmark against FeBSi AMRs and Finemet MANCs. Disseminate results. **100% Complete**

The team completed manufacturability studies on FeNi-based MANCs preceding the 12/15/21 milestone. We demonstrated manufacturability of FeCo-based components in 2022. Mechanical properties evaluation was completed 03/15/22, with additional analysis of implications for motor operation studied beyond that date. Oxide properties of AMRs and MANCs were reported at the DOE VTO June 2022 Review and summarized in **Appendix 10**. AMR and MANC testing was completed at NCSU (**App.11**) and with our commercial partner (**App.12**).

BP2 Milestone 1 was addressed for FeNi-based MANCS first due to their convenient availability and completed in 2021. The fabricability of FeCo-based AMR's was subsequently demonstrated by our commercial partner in 12/2022. Manufacturing steps were first developed in our AMO funded project and fabricability of the high power, RE-lean HSM evaluated in this project.

In BP1 we recognized the importance of epoxy impregnation on TWC fabrication and its importance in a mechanical properties, BP2 2nd Milestone. Tape Wound Core (TWC) mechanical properties reflect epoxy/oxide interfacial bonding measured by sessile drop experiments (**App. 8**) that guide vacuum impregnation bonding and inform mechanical properties evaluation. Epoxy mechanical properties were incorporated in models developed to satisfy Milestone 2. This also informed TEM (**App. 10**) in BP2 Milestone 3.

CMU Ph.d candidate, Kyle Schneider, completed analysis of mechanical properties of FeNi-based MANCs (App. 9) with the following components: (a) Mechanical Stress Modeling; (b) Model for stress induced by epoxy impregnation and curing; (c) Model for stress induced by rotation of TWC in motor application; (d) Conclusion and recommendations for future work. Work has been accepted for publication (K. Schneider, M. E. McHenry and M. P. de Boer; Strength Distributions of Laminated FeNi-Based Metal Amorphous Nanocomposite Ribbons. J. Comp. Mat. (2023). https://doi.org/10.1177/00219983231159956 (2023)).

Mechanical testing of CMU's FeNi80 base alloy was used to determine stress-strain response, including Young's Modulus (E) and Ultimate Tensile Strength (UTS). The material has high modulus but brittle failure. According to our analysis the FSWPM rotor design would incur high mechanical stresses at 15 kRPM. This high stress results from the high speed, the composite nature of the TWC rotor, and

stress concentration zones at the base of each rotor pole due to sharp internal corners. However, these high speeds are not required to achieve the power metric of 34 kW (8x power density increase over 2.5 kW reference design). Such a power density increase can be achieved with designs at lower rotational speeds. A design requiring a speed of 15 kRPM can achieve the power density requirement at the low B limit of 1.03. Since the FeNi80 alloy is now known to achieve saturation flux densities exceeding 1.3 T[7], a reduction of the required speed to 9.4 kRPM is possible, achieving the power metric.

A new method was developed to prepare tensile specimens of laminated MANC and epoxy layers, to simulate stacking of an epoxy-impregnated tape-wound core (TWC). Tensile tests were conducted for single layer ribbon and for 5- and 10- multilayer stacks of material laminated with thin layers of thermosetting epoxy. Failure distributions are quantified by Weibull statistics, (App. 9) and shown to have increasing Weibull modulus with increasing layer count. Using a *k-failure* model, we have demonstrated that *single* ribbon strength distribution data provides a good prediction of the failure distribution of 5- and 10-layer MANC ribbon laminated stacks with much improved effective ultimate tensile strength and flaw tolerance. Upon further analysis, it should be possible to assess a quantitative measure of the Figure of Safety (FOS) of component TWCs.

Because rotational stress increases with the square of the rotational speed, this speed reduction has a significant effect on the maximum stress experienced by the rotor. Nevertheless, guided by initial Figure of Safety (FOS) considerations we have limited motor rotational speeds to 6 krpm in the lab (App. 11) and comparative high f loss measurements were pursued on a smaller axial motor for the purposes of materials loss comparisons (App. 12).

After evaluating mechanical properties of FeNi-based MANCs, and concluding that standards for figures of safety (FOS) for larger diameter motors were necessary before attempting higher rotational speeds. In lieu of such tests, to evaluate loss partitioning, our project partner investigated another HSM design to allow MANC and AMR materials comparison with potentially less complicated manufacturing steps for cutting/insulation than for waterjet cut FSWPM topologies. A completed fabrication of the stator topology (App. 12) has been accomplished and loss testing is in progress. Metglas worked with a partner to construct the FeCo-based AMR rotors and stators for comparison with Fe-Ni-based MANCs in a common topology to allow direct comparison of the loss partitioning for the two materials. Materials comparisons (App. 12) in this topology are included in this final report.

Conclusions

The CMU-lead team and its partners have demonstrated pathways to 8x power density increase for RE-lean HSMs designed to showcase Amorphous Metal Ribbon (AMR) and Metal Amorphous Nanocomposite (MANC) materials. CMU presented 4 designs of a 34 kW with active mass 1.7x a 2.5 kW AMO RE-free HSM reference design. The power density is 8x compared on an active mass basis. A rotational speed < 10 krpm is predicted to achieve 34 kW. CMU work addressed (i) Materials, (ii) Manufacturing, (iii) Properties and Performance issues in new motor designs. Notable accomplishments include:

a. Adaptation of materials and manufacturing protocols for higher power HSMs.
b. Analysis of magnetostrictive coupling to residual (winding and curvature) stresses in FeNi-based MANCs and stress relief annealing protocols to further reduce losses at scale.
c. Evaluation of epoxies for impregnation bonding/electrical resistance in tape wound cores in terms of wetting, adhesion and mechanical strength.
d. FEA Modeling of Motor Mechanical Properties with identification of failure modes and methods forincreasing figures of safety.
e. Evaluation of limitations on rotor mechanical properties at high rotational speeds.

Suggestions for Future Work

We have demonstrated by theoretical analysis and prototype development that the high- power density motor with high efficiency can be realized by adoption of metal amorphous nanocomposite (MANC) materials. Flux switching permanent magnet motor with axial flux path requires low magnetic switching loss at high speeds. Our prototype MANC rotor was successfully spun to 6000 rpm and theoretical analysis indicates safe operation at 10000 rpm or higher. Our study based on 3-d finite element analysis shows that motor power can be increased by ~14 times and power density can be increased by 8 times over this 2.5 kW prototype.

Several challenges remain in commercializing this approach. We were able to fabricate rotor and stator components from MANC ribbons by toroidal core winding, heat treatments, epoxy impregnation and waterjet cutting. This method was extended to a larger motor in the completed work. However, the process is time-consuming and somewhat expensive for an industrial process. Lower cost fabrication methods need to be explored further. Higher machining precision is desired to create a machine that operates reliably at high speeds.

Our prototype motor was built to have a rotor hub structure to attach a conventional motor shaft. The MANC rotor core was encased in a structure made of glass fiber-composite. The stator that consists of MANC stator core, permanent magnets and copper coils were glued together and attached to the glass fiber-composite base that also houses the shaft bearing. The axial design has an ability to adjust the air gap between the rotor and stator. Through adjustment of the gap, the motor characteristics can be modified. Such a design should be examined more thoroughly. The motor performed as expected at low speeds but experienced resonant vibrations at high speeds. A reinforced motor housing design that also allows adjustment during assembly is highly desirable. Alignment of the dual stator's two sides and fine control of the air gaps will help meet tight specifications expected for certain applications.

We examined mechanical properties of the MANC ribbons and epoxy impregnated structure. We conclude that the developed MANC structure should perform safely at least to 10 krpm, but more experiences will be needed to establish Factors of Safety (FOS) for high speed motors. Our axial motor design has a large inner space. An innovative use of this space will make this motor more attractive. For example, a gear system may be incorporated into this space to match the high rotor speed with the required traction wheel speed.

MANC materials with higher induction are desirable in developing high power density motor. A value of 1.8 T is already achieved with commercial Co-based material. However, its high cost will preclude wide scale motor applications. We were successful in achieving 1.5T of induction based on a new composition with higher Fe and Ni contents. Presently, its coercivity is high compared with the best MANC materials and its power loss characteristics are limited. We believe these shortcomings will be overcome in the future. Our preliminary work indicates addition of a small mount (up to 10 %) of Co appears to have positive effect in improving inductions and Curie temperatures of Fe-Ni based MANC materials.

The anisotropy of MANC ribbons should be examined more carefully. The motor design usually prefers spatially uniform materials, but some designs use one-dimensional flux flow and therefore can benefit from enhanced performance in one direction. An as-cast ribbon is generally considered isotropic but because of strains in the casting process exhibit some anisotropy. We have shown significant improvements of magnetic properties by strain annealing processes in longitudinal directions but the study in transverse direction are still limited.

Key Publications

1. Y. Krimer, N. Aronhime, P. R. Ohodnicki and M. E. McHenry, Prediction of Good Glass Forming Ability in Amorphous Soft Magnetic Alloys by Thermocalc Simulation and Experimental Validation. J. Alloys and Compounds **814**,152294, (2020). https://doi.org/10.1016/j.jallcom.2019.152294
2. S. Simizu, K. Byerly, K. Schneider, H. Kim, M. Nations, S. Narasimhan, R. Beddingfield, S. Bhattacharya, & M. E. McHenry, "Flux Switching Permanent Magnet Motor with Metal Amorphous Nanocomposite Soft Magnetic Material and Rare Earth Free Permanent Magnets," 2021 IEEE Energy Conversion Congress & Exposition, Vancouver. CA, Oct. 10-14, 2021. Given Best Paper Award at ECCE 2022 Conf., Detroit, MI.
3. **K. Byerly, Y. Krimer, Charudatta Phatak, E. Theisen, and M. E. McHenry, Magnetostrictive Loss Reduction through Stress Relief Annealing in an FeNi-based Metal Amorphous Nanocomposite. J. Mat. Res. 36, 2843-55, (2021). https://doi.org/10.1557/s43578-021-00268-5.**
4. J. Egbu, P.R. Ohodnicki, J.P. Baltrus, A.Talaat, R.F. Wright and M.E. McHenry; Analysis of Surface Roughness and Oxidation of FeNi-Based Metal Amorphous Nanocomposite Alloys. JALCOM **912**, 165155, (2022).
5. K. Schneider, M. E. McHenry and M. P. de Boer; Strength Distributions of Laminated FeNi-Based Metal Amorphous Nanocomposite Ribbons. J. Comp. Mat. (2023). https://doi.org/10.1177/00219983231159956 .
6. K. Schneider, Y. Krimer, S. Simizu, M. P. de Boer and M. E. McHenry; Investigation of Metal Amorphous Nanocomposite Soft Magnetic Alloys in the $(Fe_xNi_yCo_{100-x-y})_{80}B_{14}Nb_4Si_2$ System. JALCOM 169647, https://doi.org/10.1016/j.jallcom.2023.169647 (2023).
7. **J. Egbu, A. Leary, K. Byerly, S. Simizu, P. Ohodnicki, E. Thiesen & M. McHenry; Magnetic Anisotropy and Strain Dependent Epoxy Wetting in FeNi-based Metal Amorphous Nanocomposite. Submitted to IEEE Trans. Mag. (2023).**

References

1. **M. E. McHenry, "Amorphous and Nanocomposite Magnets for High Efficiency, High Speed Motor Designs". USDOE Technical Report. (2021). https://doi.org/10.2172/1828188. https://www.osti.gov/servlets/purl/1828188.**
2. S. Simizu, K. Byerly, K. Schneider, H. Kim, M. Nations, S. Narasimhan, R. Beddingfield, S. Bhattacharya, and M. E. McHenry, "Flux Switching Permanent Magnet Motor with Metal Amorphous Nanocomposite Soft Magnetic Material and Rare Earth Free Permanent Magnets," presented IEEE Energy Conversion Congress and Exposition 2021, Vancouver. Canada, Oct. 10-14, 2021. This was awarded Best Paper Award at ECCE 2022, Detroit, Mi.
3. M. E. McHenry, M.A. Willard, and D.E. Laughlin, Amorphous and Nanocrystalline Materials for Applications as Soft Magnets. Prog. Mat. Sci. **44**, 291-433, (1999). (http://dx.doi.org/10.1016/S0079-6425(99)00002-X).
4. M. E. McHenry and D. E. Laughlin; Chapter 19 - Magnetic Properties of Metals and Alloys. **Physical Metallurgy** - 5th Ed., Elsevier B.V. 1881–2008, (2015). http://dx.doi.org/10.1016/B978-0-444-53770-6.00019-8
5. N. Aronhime, V. DeGeorge, V. Keylin, P. Ohodnicki, and M. E. McHenry, "The Effects of Strain-Annealing on Tuning Permeability and Lowering Losses in Fe-Ni-based Metal Amorphous Nanocomposites." J. Materials **69(11)**, 2164-70, (2017). 10.1007/s11837-017-2480-x
6. **K. Byerly, Y. Krimer, Charudatta Phatak, E. Theisen, and M. E. McHenry, Magnetostrictive Loss Reduction through Stress Relief Annealing in an FeNi-based Metal Amorphous Nanocomposite. J. Mat. Res. 36, 2843-55, (2021). https://doi.org/10.1557/s43578-021-00268-5.**
7. Y. Krimer, N. Aronhime, P. R. Ohodnicki and M. E. McHenry, Prediction of Good Glass Forming Ability in Amorphous Soft Magnetic Alloys by Thermocalc Simulation and Experimental Validation. J. Alloys and Compounds **814**,152294, (2020).

https://doi.org/10.1016/j.jallcom.2019.152294

8. J. Egbu, P. R. Ohodnicki, J. P. Baltrus, A. Talaat, R.F. Wright and M. E. McHenry; Analysis of Surface Roughness and Oxidation of FeNi-Based Metal Amorphous Nanocomposite Alloys. J. Alloys & Compounds **912**, 165155, (2022).

Acknowledgements:

We gratefully acknowledge the DOE Advanced Manufacturing Office (AMO) under Agreement DE-EE0007867 and the DOE Vehicle Technology Office (VTO) under Agreement DE-EE0008870.

The team thanks the DOE's Susan Rogers, John Tabacchi and Benjamin May as well as their staffs for their oversight of this project and the DOE for funding the work under: DOE/EERE/VTO; DE-EE0008870

The team thanks the many staff and support personnel who have contributed to the project, especially during the trying times posed throughout the pandemic. We call out, in particular, Anthony Talotta for his tireless efforts in facilitating Project financial management.

The team gratefully acknowledges: (1) A CMU/Metglas research use license agreement (RULA) allowing production of scaled 1 and 2' wide ribbons of FeNi-based MANCs used in TWCs for subsequent fabrication steps; (2) OMAX demonstration of rotor and stator waterjet cuts required for our 34 kW motor design; Quadrant's provision of Dy-free NdFeB permanent magnets in sector geometries for the 34 kW motor design; (3) Spang Engineered Systems (SES) provided bobbinless Cu coils in geometries required for our 34 kW motor design; (4) Kevin Byerly who was hired by CMU to work on HSM design, component evaluation, and protocols developed to reduce magnetoelastic losses. He has since joined CorePower Magnetics. (6) North Carolina State University (NCSU) personnel built a test stand to evaluate motor performance at high rotational speeds. (7) Metglas personnel who accomplished FeCo-based stator fabrication and materials comparisons.

Appendices

Appendix 1: Project Personnel

Principal Investigator:	Michael McHenry, 412-268-2703,	mm7g@andrew.cmu.edu
CMU Co-Investigator:	Maarten De Boer, 412 268 8752,	mpdebo@andrew.cmu.edu
CMU Senior Scientist:	Satoru Simizu	simizu@andrew.cmu.edu
CMU Visiting Scientist:	George Bellesis	gbellesi@andrew.cmu.edu
Graduate Students:	Materials Science and Eng.:	Yuval Krimer, James Egbu,
	Mechanical Eng.:	Kyle Schneider, Walter Robinson

Business Contacts:

Rebecca Harrold,	412-268-4061,	rebeccap@andrew.cmu.edu
Anthony Talotta.	412 268 5765,	atalotta@andrew.cmu.edu
Eric Theisen,	843-349-7319	Eric.Theisen@metglas.com

Partners:

NCSU:	Subhashish Bhattacharya,	sbatta4@ncsu.edu
Metglas:	Eric Theisen,	Eric.Theisen@metglas.com

DOE VTO:

John G. Tabacchi, NETL	John.Tabacchi@NETL.DOE.GOV
Amanda Lopez, NETL	Amanda.Lopez@NETL.DOE.GOV
Susan Rogers, DOE EE	susan.rogers@ee.doe.gov

Industry Advisors:

Eric Theisen,	Metglas	Eric.Theisen@metglas.com
Natan Aronhime,	Carpenter	NAronhime@cartech.com

Appendix 2: Metglas AMR Alloy Short Brochure

Metglas®

Magnetic Materials Catalog

www.metglas.com *Cobalt, Iron, Iron-Nickel Amorphous and Iron Nanocrystalline*

Metglas® has a family of soft magnetic alloys engineered to suit your design needs. The data below compares the properties of each alloy.

1. Physical Properties

Metglas Alloy	Nominal Composition	Thickness (microns)	Saturation Induction (T)	Density (g/cm^3)	Curie Temp (C)	Crystalization Onset (C)	Magneto-striction (ppm)	Lamination Factor (%)
2714A	CoFeSiNiB	15	0.60	7.59	225	550	< 1	79
2705M	CoFeSiNiBMo	22	0.77	7.80	365	520	< 1	79
2826MB3	NiFeBMo	28	0.90	7.90	360	409	11	85
FT-3	FeBSiNbCu	17	1.20	7.30	570	510	< 1	75
2605S3A	FeCrBSi	23	1.45	7.29	358	535	20	82
2605SA1	FeBSi	23	1.56	7.18	395	510	27	89
2605HB1M	FeBSi	25	1.63	7.33	364	489	27	89
2605CO	FeCoBSi	23	1.80	7.56	415	430	33	84

2. DC Magnetic Properties

The DC soft magnetic properties of each alloy are shown below. Data is given in the as-cast state and after magnetic field annealing.

Metglas Alloy	Induction @ B800 (T)		Remnant Induction @ B800 (T)		Coercivity, Hc (A/m)		Max Relative Permeability	
	As-cast	Annealed	As-cast	Annealed	As-cast	Annealed	As-cast	Annealed
2714A	0.59	0.60	0.41	0.58	1.0	0.2	240,000	4,200,000
2705M	NA	0.76	NA	0.75	NA	0.7	NA	1,300,000
2826MB3	0.70	0.90	0.25	0.89	3.6	0.5	38,000	2,100,000
FT-3	NA	1.20	NA	0.71	NA	0.9	NA	410,000
2605S3A	1.27	1.44	0.53	1.30	5.3	0.6	47,000	1,300,000
2605SA1	1.36	1.57	0.61	1.48	5.7	1.0	52,000	1,100,000
2605HB1M	1.46	1.62	0.73	1.53	3.7	0.9	141,000	1,117,000
2605CO	1.66	1.78	1.15	1.71	3.8	1.8	110,000	750,000

Appendix 3: Metglas High Induction Alloy 2605CO

Metglas®

Magnetic Alloy 2605CO(Iron-based)

www.metglas.com

Technical Bulletin

Applications

- Pulse power devices
- Airborne transformers

Benefits

- Highest saturation induction of any amorphous alloy commercially available

- Extremely low core loss – at 1.6 Tesla, 400 Hz,are less than half those of 4 mil 3% silicon-iron• Can be annealed for very high squareness ratio

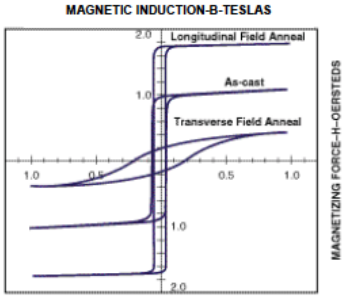

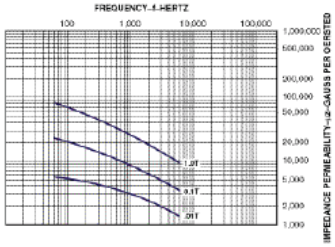

Physical Properties	
Density (g/cm³)	7.56
Vicker's Hardness (50g load)	810
Tensil Strength (GPa)	1-2
Elastic Modulus (GPa)	100-110
Lamination Factor (%)	>75
Thermal Expansion (ppm/°C)	8.6
Crystallization Temperature (°C)	430
Continuous Service Temp. (°C)	125

Magnetic Properties	
Saturation Induction (T)	1.80
Maximum D.C. Permeability (μ):	
Annealed	400,000
As Cast	120,000
Saturation Magnetostriction (ppm)	35
Electrical Resistivity (μ-cm)	123
Curie Temperature (°C)	415

Appendix 4: Preliminary Motor Design

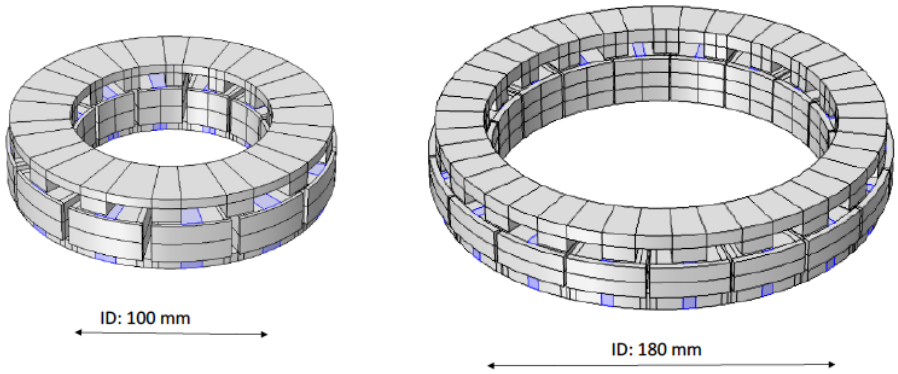

Fig. A4.1: Dual stator 2.5 kW FSWPM HSM design (left) and proposed > 20 kW HSM Design (right).

Enhancing specific power

Parameters	Initial (with verified material properties)	High power (with projected material properties)
Electrical Speed (at 6000 rpm)	1400 Hz	2100 Hz
Inner radius/outer radius	50 mm/80 mm	90 mm/115 mm
Flux density (peak)	0.60 T	1.53 T
Permanent magnet	Ferrite (B_r = 0.4 T)	NdFeB (B_r = 1.2T)
Current density (peak)	6.0 A/mm^2	18.0 A/mm^2
Conductor filling factor	46 %	60 %
Torque	4.2 Nm	59 Nm
Power (at 6000 rpm)	2.6 kW	37 kW
Copper loss (DC)	34 W (1.3 %)	230 W (1.3 %)
Iron loss (at 6000 rpm)	7 W (0.3 %)	82 W (0.2 %)
Motor mass	5.8 kg	9.9 kg
Specific power	0.45 kW/kg	3.8 kW/kg

Table A4.1: Engineering parameters of dual stator 2.5 kW FSWPM HSM (Initial, left) and proposed >20 kW HSM Design (High Power, right).

Appendix 5: Alloy Development Summary

Alloys were produced in the $(Fe_{70}\ Ni_{30})_x(B\text{-}Si\text{-}Nb)_{100\text{-}x}$ series for x=82, with compositions $(Fe_{70}Ni_{30})_{82}Nb_1Si_1B_{16}$, $(Fe_{70}Ni_{30})_{82}Nb_2Si_0B_{16}$, and $(Fe_{70}Ni_{30})_{82}Nb_3Si_0B_{15}$. An additional x=85 alloy was produced:$(Fe_{70}Ni_{30})_{85}Nb_{05}Si_0B_{14.5}$. All alloys were melted 3 times in Ar in a Centorr Vacuum Industries Series 5 furnace, and planar flow cast in an Edmund-Buhler Sc melt spinner at a 35 m/s wheel speed and 1 mm nozzle size. Samples were cut in 0.025-0.035 g pieces and measured in a Perkin Elmer DSC 8500 (in Ar) to 700 °C at a 40 °C/min heating rate to determine Curie temperature (T_c), T_g, and T_x. T_c measurements were confirmed using a Quantum Design PPMS magnetometer heating to 800 K at 20 K/s in a 200 Oe field. Saturation Induction was also measured the PPMS magnetometer. 3.5 mm wide ribbon was also melt-spun using a wheel speed reduced to 31.8 m/s. Samples were annealed at 415-445 °C after encapsulation in Ar. XRD measurements were used to determine crystallization products. A sample of as cast and 415 °C annealed sample was tested on a Laboratorio Elettrofisico Automatic Magnetic Hysteresisgraph for saturation induction and coercivity.

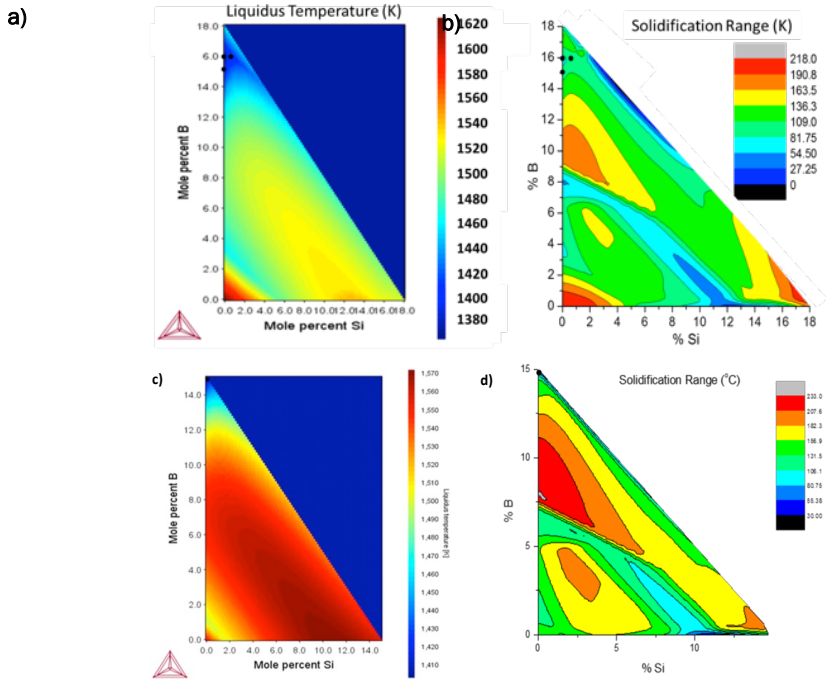

Fig. A5.1. (a) liquidus temperature and (b) solidification range of the x=82% alloys. (c) Liquidus temperature and (d) solidification range of the x=85% alloys.

Fig. A5.1a and **A5.1b** Thermocalc simulation results for the x=82% alloy system (dots showing alloys produced). A region with a minimum in liquidus is seen at 15-17% B and 0-5% Si. The corresponding minimum in solidification range is small, Fig. A5.2b. The 3 compositions

were all successfully cast as continuous ribbon and confirmed to be amorphous by a bend test. **Fig. A5.1c** and **A5.1d** show Thermocalc results for the x=85% alloy. As seen in the figure, the region with a minimum in both liquidus and solidification range is very small. Nonetheless one alloy successfully cast, and confirmed amorphous by a bend test.

Magnetic properties are summarized in **Table A5.1**. Curie temperatures of the amorphous phase ranged from 407 to 438 °C for the x=82% alloys and 462 °C for the x=85% alloy, shown to increase with magnetic element concentration. Saturation induction of the as-cast samples were 1.28-1.36 T for the x=82% alloys, and 1.48 T for the x=85% alloys. The saturation induction of previously developed $(Fe_{70}Ni_{30})_{80}Nb_4Si_2B_{14}$ was ~1.3 T when annealed. The saturation induction of the x=85% alloy shows substantial improvement over the previously developed alloy. Coercivity was higher than optimal, and this believed to be due to magnetostrictive losses. Annealing was suggested to relieve stress and reduce coercivity.

	$(Fe_{70}Ni_{30})_{82}B_{15}Si_0Nb_3$	$(Fe_{70}Ni_{30})_{82}B_{16}Si_0Nb_2$	$(Fe_{70}Ni_{30})_{82}B_{16}Si_1Nb_1$	$(Fe_{70}Ni_{30})_{85}B_{14.5}Nb_{0.5}Si_0$
$T_{c(amorphous)}$ (°C)	407	417	438	462
B (Tesla)	1.32	1.36	1.28	1.48
H_c (A/m)	37.6	30.0	30.7	26.0

Table A5.1: Curie temperature, saturation induction, and coercivity of the as-cast alloys.

Fig. A5.2(a) shows M(T) for an x=85% alloy to initially decreases with T, as the amorphous phase T_c is approached. It subsequently increases with crystallization. An increase in one measurement increment is unusual. Typically such a steep increase occurs in polymorphic crystallization. XRD was performed on samples annealed at 415-445 °C shown in **Fig. A5.2(b)**. A 2-step crystallization: Amorphous → BCC+FCC+Amorphous → BCC+FCC+Fe_3B+$Fe_{23}B_6$ was observed. 415 °C annealing was chosen to optimize magnetic properties.

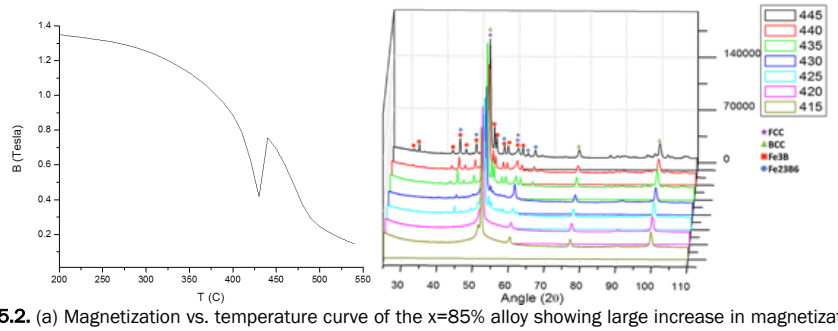

Fig. A5.2. (a) Magnetization vs. temperature curve of the x=85% alloy showing large increase in magnetization with crystallization. (b) XRD results of the x=85% alloy annealed at increasing temperatures, showing a 2-step crystallization process of Amorphous → BCC+FCC+Amorphous → BCC+FCC+Fe_3B+$Fe_{23}B_6$.

Fig. A5.3 shows strip testing results of the annealed and as-cast ribbons of this alloy. Saturation induction of the as-cast alloy increased from 1.43 T for the as-cast to 1.53 T for the annealed sample. Additionally, the B-H loop is more square but coercivity increased to 114 A/m, high for a nanocrystalline material. The high coercivity is believed to result of from

crystal coarsening. A Nb content of 0.5%, limits its inhibition of grain growth. Annealing 0.5 hours at the annealing temperature allowed time for crystal growth. Rapid annealing to allow crystallization without time for excessive grain growth, may improve properties. Rapid annealing has been explored for nanocrystalline alloys with low growth inhibitor content. It can limit grain size to <20 nm even in alloys without transition metal growth inhibitors, e.g. Nb.

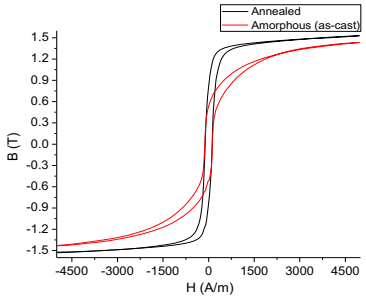

Fig. A5.4. Strip testing result of the as-cast and annealed 3.5 mm ribbon in x=85 alloy.

Table A5.2 lists glass transition temperatures, primary crystallization temperatures, and ΔT_{xg} values. ΔT_{xg} ranges from 12-23 °C. For the x=85% alloy, the T-range is 20 °C, which should be sufficient for hot stamping. A more rapid heating rate shifts Tx_1 up, allowing larger formability.

	$(Fe_{70}Ni_{30})_{82}B_{15}Si_0Nb_3$	$(Fe_{70}Ni_{30})_{82}B_{16}Si_0Nb_2$	$(Fe_{70}Ni_{30})_{82}B_{16}Si_1Nb_1$	$(Fe_{70}Ni_{30})_{85}B_{14.5}Nb_{0.5}Si_0$
T_g (°C)	420	431	421	399
T_{x1} (°C)	438	443	444	419
ΔT_{xg} (°C)	18	12	23	20

Table A5.2: Glass transition, primary crystallization temperatures, and supercooled liquid range for tested alloys.

Magnetic properties were also investigated in an as-cast 50mm wide (FeNi)85% alloy produced by Metglas. Strip and core measurements identified B-H loop characteristics. A Laboratorio Elettrofisico AMH-50K-S AC/DC Hysteresis-graph was used with a single strip test fixture (**Fig. A5.5**). This test fixture consists of a laminated yoke and an excitation/measurement coil containing both primary (H) and secondary (B) windings.

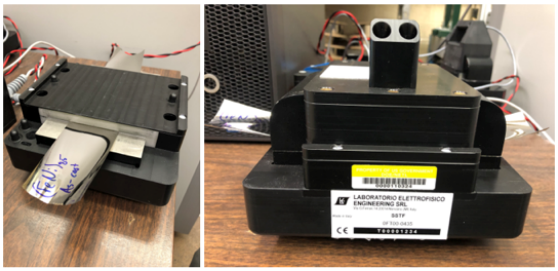

Fig. A5.5: Strip testing setup for as-cast 50mm wide ribbon.

Induction (B) and magnetic field (H) are measured to determine values of permeability, coercivity, and B-H loop shape. Strip measurements were compared with a wound core of dimension 38.1mm OD x 25.4mm ID. The core was prepared for testing by placing it inside a 3D printed box and wound with primary and secondary windings (**Fig. A5.6**).

Fig. A5.6: Core winding and testing of 50 mm wide ribbon.

An automated sequence was run at 400Hz from 0.1T to 1.5T on the strip and from 0.1T to 1.0T on the core. Magnetic properties results are given below, including AC losses, coercivity, and B-H loop square factor Kr (**Fig. A5.7 and A5.8**). It is noted that strip and core properties differ due to magnetostrictive coupling (i.e. bending stresses are introduced when shaping the strip into a toroid). Further optimization by stress relief annealing to reduce magnetostrictive effects and increase induction are discussed in subsequent research below.

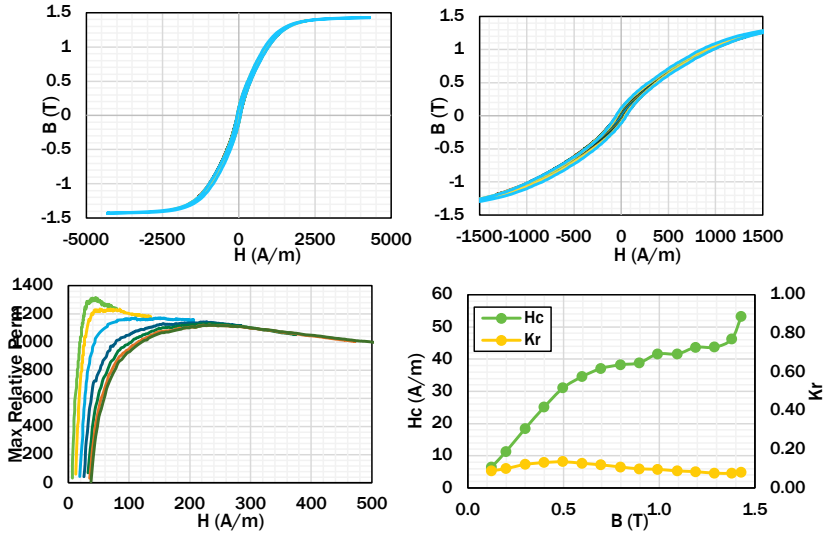

Fig. A5.7. As-cast strip measurements at 400Hz. Bs of the as-cast strip is 1.43T.

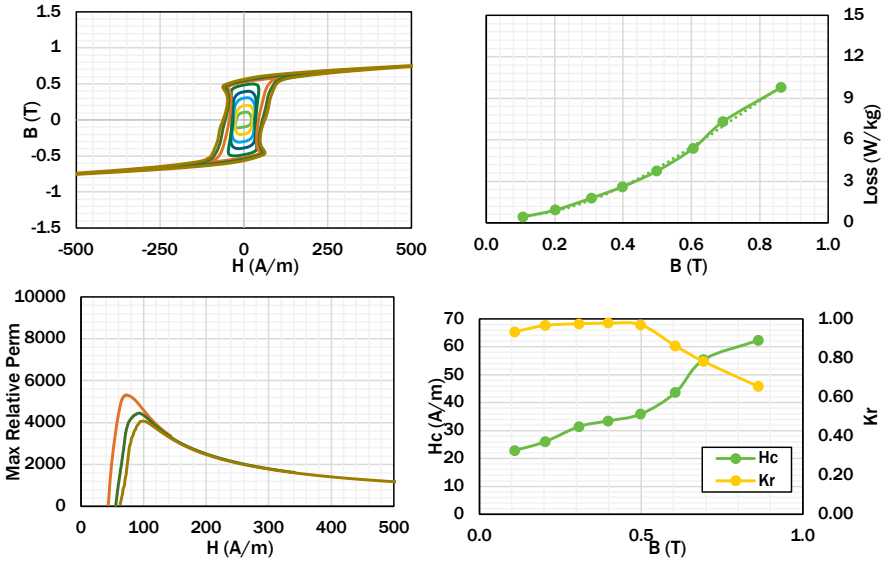

Figure A5.8. As-cast core measurements at 400Hz. AC losses at 1T = 12.13W/kg (extrapolated).

Fig. A5.9 compares as-cast strip and core loss results for the (FeNi)85% alloy.

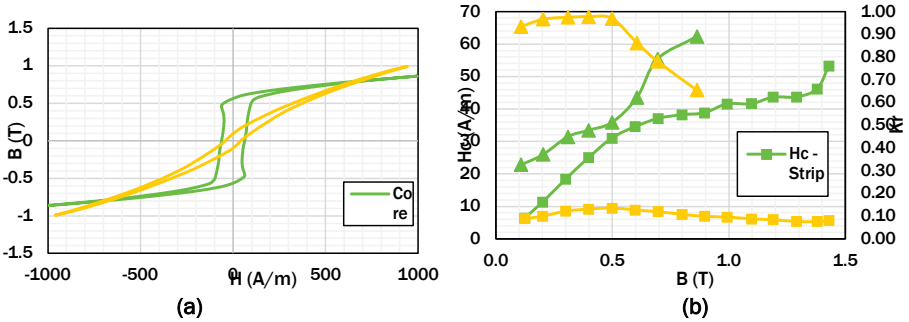

Figure A5.9: (a) B-H loop shape and (b) coercivity (Hc), and square factor (Kr) comparison at 400Hz between the as-cast strip and core for the (FeNi)85% alloy.

Optimized Annealing to Improve Magnetic Properties of (FeNi)80%

Alloys with large inductions required for motors often do not have magnetostriction coefficients sufficiently small for low high frequency loss. Thus, loss reduction must be pursued through core processing and anneal optimization. Investigating annealing treatments over a range of conditions (varying time, temperature, and external fields) can locate optimal point(s).

We investigated strain annealing to demonstrate permeability tuning for motor applications. In such an annealing process, the ribbon is flat and held under tension while

passed through a furnace thermal heating zone (see **Fig. A5.10**). Once the ribbon is gathered it is then wound into a toroidal core. Dramatic changes in properties are observed before and after winding. The effects are determined to be of magnetostrictive origin and, thus, a procedure was developed to re-anneal for stress relief. A systematic set of re-annealing was performed between 300 and 470^{0}C and a minimum for AC core loss and coercivity was identified at 450 C, 30 min. Optimized (FeNi)80% core loss results are (**Fig. A5.11)** were benchmarked with FINEMET and 2605CO.

(a)  (b) 

Fig. A5.10: (a) Strain annealing machine setup with view of annealing furnace and rewind station, (b) wound toroidal cores (31.75mm x 25.4mm) using the strain annealed ribbon.

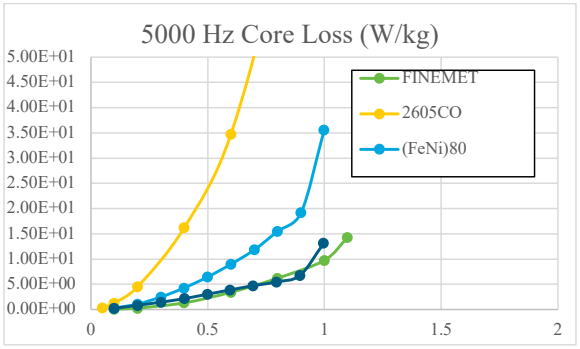

Fig. A5.11: Core loss (W/kg) vs. induction (T) measured at 5kHz. An (FeNi)80% alloy exhibits optimal magnetic properties comparable to state-of-the-art FINEMET materials. Although the 2605CO material has a higher B_{sat}, the losses are roughly 25X higher at 1T.

Comparison of wide AMR and MANC ribbon at 5kHz

AC soft magnetic properties of ***Metglas 2605CO*** and ***CMU (FeNi)80%*** were evaluated at 5kHz. Data was collected over a range of induction levels for toroidal core samples annealed under (1) no field and (2) applied field conditions. Annealing in zero field involves only a thermal treatment. Annealing under field conditions involves a selection of either magnetic or mechanical (strain) fields coupled with a thermal treatment.

For field annealing the 2605CO alloy, a DC magnetic field is directed along the long axis of the ribbon during thermal treatment to release stress and induce the magnetic anisotropy along the long axis of the ribbon. This is known as longitudinal field (LF) annealing.

The (FeNi)80 alloy, undergoes an in-line strain annealing (SA) process to induce anisotropy and further tailor the B-H loop. During the SA process, flat, continuous ribbon is passed through a furnace section under tension. (Note that the FeNi material requires heat treatment for nanocrystallization; the 2605CO alloy is used in its amorphous state.) After this process, the ribbon is wound into a core. Magnetostrictive effects from core winding require post-treatment similar fashion to thermal treatment only for final magnetic properties optimization.

Fig. A.5.12(a) illustrates B-H loop shapes. For the 2605CO alloy annealed under no field, a maximum relative permeability of ~4500 was measured at H = 100 A/m. The value of permeability at the vertex of the B-H loop measures ~1800, representing a change in slope as the core approaches saturation. The squareness factor K_r, defined as the ratio of the remanence B_r and saturation B_s induction, measures 0.75, classifying this as a square loop material. LFA annealed cores (not pictured) exhibit high K_r, values >0.90, corresponding to almost a complete retention of induction as AC power is cycled.

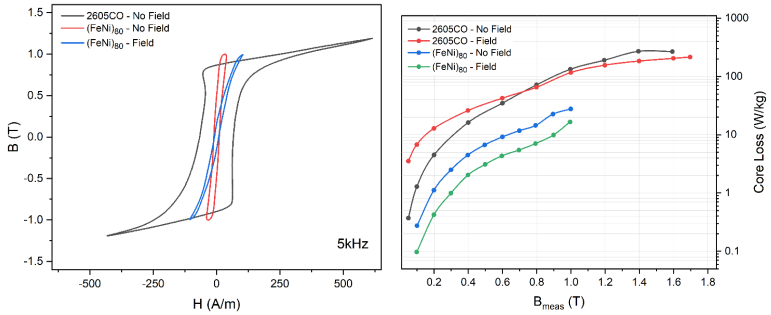

Fig. A5.12: (a) B-H loops at 5kHz for Metglas 2605CO alloy (no field) as compared to CMU's (FeNi)80 alloy with and without mechanical field (strain) annealing; (b) 5kHz core loss as a function of induction for Metglas 2605CO and CMU (FeNi)80 alloys annealed under 0 field and field conditions.

For the (FeNi)80 alloy, B-H loops are much flatter, with a squareness, K_r <0.50 for 0 field and ~K_r ~ 0.10 for SA (field) conditions. Maximum permeabilities of ~20,000 & ~10,000 was measured on in 0 field and field annealed core samples, respectively. The values of permeability at the vertex of the B-H loops are nearly equivalent to the maximum permeability since the cores were not driven to full saturation. We expect a similar roll-off in permeability during approach to saturation (B_s = 1.2T).

Fig. A5.12(b) shows core loss as a function of increasing induction levels for both alloys. Longitudinal field annealed 2605CO cores exhibit only an incrementally smaller loss at higher inductions (>0.8T) as compared to 0 field annealing. Strain annealed (FeNi)80 cores exhibit a 50% reduction as compared to 0 field annealing for the entire range of inductions.

In summary, the 2605CO alloy has superior saturation induction (B_s = 1.8T), but the high-f losses (5kHz) are ~an order of magnitude higher than (FeNi)80. The (FeNi)80 alloy exhibit more controllable magnetic properties at high-f, making it more attractive to applications such as HSMs and power transformers. Metglas provided several full-length casts of the (FeNi)80% alloy in 1" wide ribbon. CMU staff worked with Dr. Eric Theisen of Metglas to optimize casting conditions and to give feedback of magnetic/mechanical properties. This alloy is of significant interest due to excellent (1) mechanical properties after nanocrystallization, (2) high-f soft magnetic properties: low core loss, high saturation magnetic flux density, high permeability and (3) flexibility to control B-H loop shape during annealing.

Appendix 6: Evaluation of Magnetostriction in AMR and MANC Alloys.

CMU Method for Physical Property Validation: To test magnetostriction, a measurement system was developed at CMU using strain gauges applied to (1) ribbons & (2) wound cores. Applying a DC current to a coil encircling the material, a static magnetic field is applied and the measured strain at the saturating field yields the saturation magnetostriction, λ_s. This method was used for both tape wound cores (**Fig. A6.1**) and single, straight strips of ribbon (**Fig. A6.2**). In using the straight strip measurement method, a cut magnetic core of high permeability is used to complete the magnetic path with low reluctance. Clamping two halves of the cut core onto the ribbon creates good contact between the ribbon and core to minimize magnetic fringing. Knowing the magnetic path length allows for ease in calculating field.

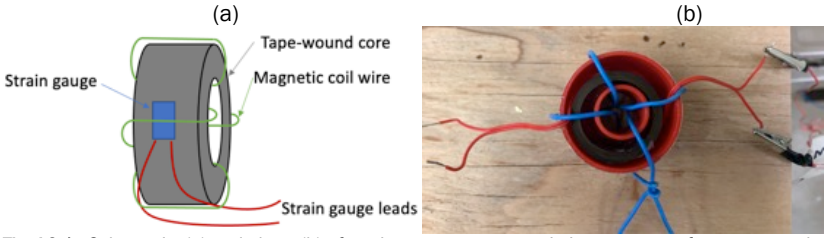

Fig. A6.1: Schematic (a) and photo (b) of strain gauge magnetostriction test setup for tape-wound cores.

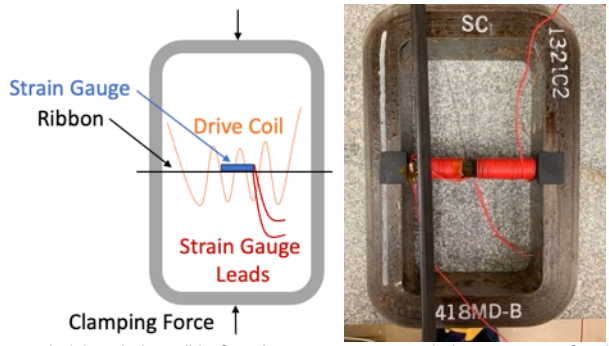

Fig. A6.2: Schematic (a) and photo (b) of strain gauge magnetostriction test setup for single strips.

Strain gauge measurements were taken using a Micro Measurements MM01 MultiDAQ Datalogger and a Windows program. In both, a 120Ω strain gauge was bonded to the ribbon using a strain gauge adhesive and covered with Kapton tape. Strain gauge leads were connected to a 3-wire Quarter Wheatstone Bridge in the MM01 MultiDAQ. In both configurations, the magnetic path length is measured, and the number of coil turns counted. These values are used to calculate the DC current required to provide a magnetic field sufficient to saturate the material (**Eqn, 1**) where H is the applied field, I is current, N is number of coil turns, and L is the magnetic path length). MultiDAQ datalogging software was modified to allow applied magnetic field to be shown real time on the monitoring computer.

Because many strain gauges are sensitive to magnetic fields, a “dummy gauge” is used to detect this effect. This dummy gauge is placed next to the bonded gauge on the ribbon, but not affixed to the material with strain gauge adhesive. The strain reading present when the field is applied is then recorded and subtracted from the strain reading from the bonded gauge to account for field-dependent strain gauge offset.

$$H = \frac{IN}{L} \qquad (1)$$

The method was used to measure magnetostriction for Metglas 2605CO (Fe-based) and Metglas-cast (FeNi)80% MANC alloys. **Table A6.1** compares results of these tests with the magnetostriction of each alloy reported by Metglas. Two alloys with known magnetostriction were used to calibrate the new system. The system records strain (and by inference magnetostriction) to $1x10^{-6}$ (1 ppm) precision. **Fig. A6.3** shows full system setup with real-time chart monitoring and data-logging software.

	Metglas λ_s Value (ppm)	CMU λ_s Value (ppm)	% Difference
(FeNi)80% Core	-10	-10	0.00%
2605CO Strip	33	36	-9.09%

Table A6.1: Magnetostriction comparison table

(a) 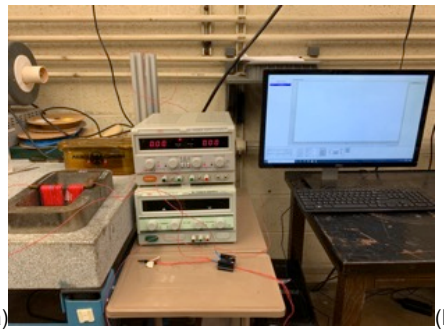 (b) 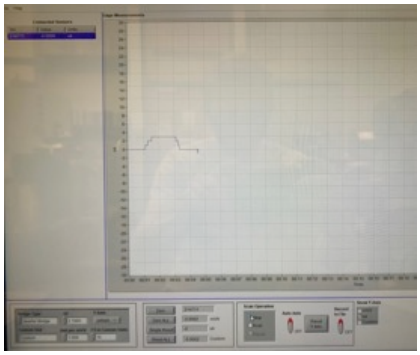

Fig. A6.3: (a) Magnetostriction test setup for single, strip test fixture (left), DC power supply for coil current (center) and data-logging PC (right) and (b) screenshot of real-time field-dependent magnetostriction.

Metglas Magnetostriction Method and Results:

Metglas uses a similar strain gauge method to test magnetostriction. A gauge was glued and mounted to a ribbon to be tested (**Fig. A6.4**). Ribbon samples were saturated in an applied DC field (generated between two large electromagnets). The sample was rotated in the DC field where high and low voltage measurements are taken at two orientations, 90° apart (along the ribbon width and length). Both (FeNi)80% and (FeNi)85% alloys were tested, and reported in **Table A6.2**

(a)  (b) 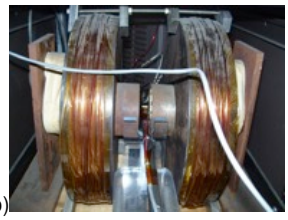 (c) 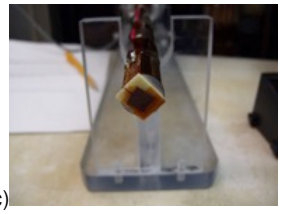

Figure A6.4: (a) Ribbon sample preparation with strain gauge, (b) electromagnet, and (c) sample rod.

Sample	High 1 (uV)	Low 1 (uV)	High 2 (uV)	Low 2 (uV)	Max (uV)	Min (uV)	Vr	λ_s (ppm)
(FeNi)80% as-cast	373	349	364	347	373	347	0.000013	18.6
(FeNi)80% annealed	1017	1003	1016	1003	1017	1003	7E-06	10.0
(FeNi)85% as-cast	925	905	924	904	925	904	1.05E-05	15.1
(FeNi)85% annealed	471	448	470	449	471	448	1.15E-05	16.5*

Table A6.2: As-cast vs. annealed magnetostriction in (FeNi)-based MANC alloys. *Not optimal heat treatment.

Appendix 7: Power Density Improvement Evaluation with AMRs and MANCs.

The FSWPM motor requires a high magnetic switching rate because of high pole counts of the rotor. In our design, the pole number is 18 and the magnetic switching rate is 18x that of the mechanical rotational speed. Even for a modest speed of 100 Hz mechanical speed (6000 rpm), the magnetic switching rate is 1800 Hz. Such a high rate could cause a very significant power loss. We have examined several AMR/MANC materials to determine if existing or emerging materials can meet loss metric requirements. Co-based AMRs and FeNi-based MANCS were benchmarked against other MANCs and results summarized here.

Table 7.1 shows the frequency limit for several materials when the power loss is set at 10 W/kg at 1 T of flux density. With Si Steel, this limit is reach at 150 Hz. 2605CO is a commercially available AMR and its saturation flux density exceeds 1.6 T. The limit frequency is about 1 kHz. FeNi-80 is an MANC alloy developed by us showing very low power loss and good mechanical properties. The frequency limit is extended to 3 kHz. Finemet, which is generally considered to be lowest loss amorphous metal shows even better loss characteristics and the frequency limit reaches 5 kHz. However, Finemet is mechanically fragile and is not currently considered for motor applications.

Our results are based power loss determination from B-H loop measurements as applied to 3-D FEA models. In one model (1 T design), flux densities are limited to 1 T. Thus, the model can accommodate any of the 4 SMMs. **Table A7.1** shows maximum power of the motor when driven to the frequency limit. Another model (1.7 T design) is only feasible with Si Steel and 2605CO. It is noted that a variant of FeNi-80 that is aimed to achieve higher flux density while retaining the low power loss has been developed and already showing a promise. FeNi-80 has already satisfied requirements for developing 20 and 34 kW designs.

Table A7.1. Comparison of SMM candidates for the high-speed motor design.

SMM	Frequency limit (10 W/kg loss)	1 T design	1.7 T design	Comments
Si Steel	150 Hz	1.0 kW	2.7 kW	
2605CO	1 kHz	6.7 kW	18 kW	
FeNi-80	3 kHz	20 kW		
Finemet	5 kHz	33 kW		Fragile

We developed 4 designs of 34 kW motor with varied magnetic flux levels of the soft magnetic material (SMM). For all 4 designs, the active mass is 1.7 times the reference 2.5 kW motor. The power density of the 4 designs shows an increase of 8x power density compared on an active mass basis. Design parameters are listed in **Table A7.2**. With Designs 1&2, the flux densities are 1.8 and 1.4 T. These can be achieved with 2605CO (Metglas). A rotational

Table A7.2. Four 34 kW designs with 8x power density of the 2.5 kW reference motor.

Design	1	2	3	4
Flux density (T)	1.76	1.38	1.17	1.03
SMM	2605CO	2605CO	FeNi-80	FeNi-80
Torque (Nm)	57.8	39.4	28.6	21.6
Rotational Speed (rpm)	5620	8240	11400	15000
Electrical Speed (Hz)	1970	2880	3980	5270
Iron loss (W)	230	260	58	69
Copper loss (W)	400	400	400	400

speed less than 10 krpm achieves 34 kW. Expected iron loss is relatively high at 230 W and 260 W for Design 1&2 but still lower than the Cu loss of 400 W. We can adopt FeNi-80 MANC for Designs 3&4. Because of lower flux density, the torque is lower and 34 kW power is achieved only at higher speeds. The iron loss is low even at these high speeds.

Rotor rotational stress increases rapidly with rotation speed. **Table 7.3** calculates maximum stress for radial and tangential directions as compared with yield strength. Radial stress should be compared with the epoxy resin strength supporting the epoxy impregnated body. The tangential stress is primarily supported by the ribbon. The analysis indicates the rotor should be able to withstand rotational stresses for speeds assumed for the 4 designs.

Table A7.3. Calculated rotational stress in the rotor

Rotational speed (rpm)	Max. Radial stress (MPa)	Max. Tangential stress (MPa)
6000	0.66	32
15000	4.2	200
30000	16.6	790
Yield strength	30 ~ 120 (epoxy)	1000 ~ 1400 (ribbon)

design parameters	unit	comments	Values
NS		no. of slots	18
NR		no. of rotor tips	21
R1	mm	inner radius	90
R2	mm	outer radius	115
gap	mm	axial air gap length	1 ~ 2
hRt	mm	height, rotor tip	6
hRr	mm	height, flux return path	9
hSt	mm	height, stator tip	17
hSr	mm	height, flux return path	9
height	mm	total, dual stator	84 ~ 86
xRt	fraction	rotor tip	0.48
xmag	fraction	magnet	0.15
xslot	fraction	slot width	0.20
fx	fraction	coil filling factor	0.60
Acoil	mm^2	filled area	32
lcoil	mm	length	2446

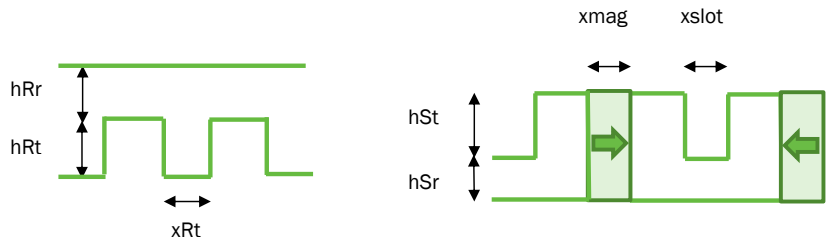

Fig. A7.1: Design Geometry Details for 34 kW FSWPM Motor

Fig. A7.1 summarizes and further illustrates design parameters for a 34 kW FSWPM motor.

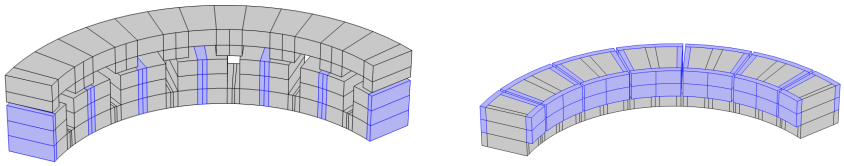

(a) (b)

Fig. 7.2: 3-d FEA model (a) Stator without coils & rotor, (b) Stator without coils (both 1/3 model.

Fig. 7.2 illustrates a 3-d FEA model of (a) Stator without coils & rotor, (b) Stator without coils (both 1/3 model, as manufactured from a MANC coil by waterjet cutting, **Fig.7.3**. **Fig. 7.4** shows a wound core, after waterjet cutting, wrapped with thermally cured reinforcing tape.

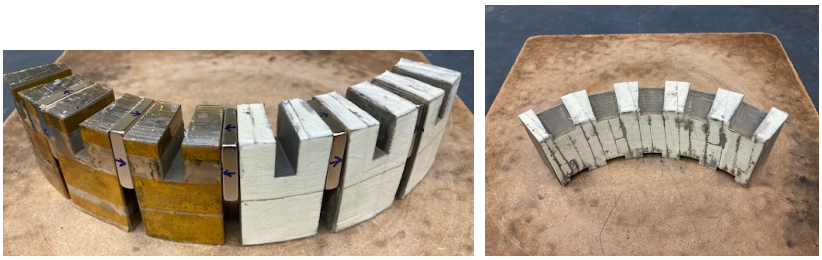

Fig. A7.3: Partial Assembly with FeNi-MANC ribbon core (a) Partial stator assembly with PM polarity shown by arrows (5 magnets +6 wedges) (b) waterjet cutting of the rotor slots

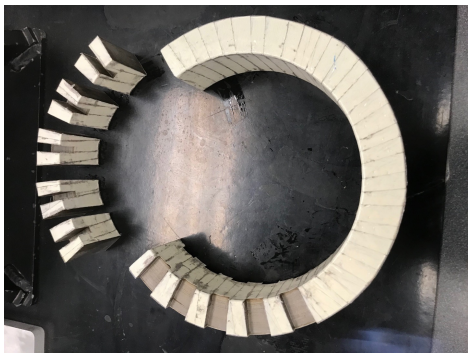

Fig. A7.4: After waterjet cutting. Wound core is wrapped with a (thermally cured) tape for reinforcing.

Appendix 8: Sessile Drop Wetting Experiments.

James Egbu built an apparatus to measure the contact angle of a liquid droplet on sample to study surface energy by sessile drop experiments with a camera wand upgraded lens mounted on a linear stage. **Fig. A8.1(a)**. An epoxy sample (deposited by syringe) sits on a tilting stage mounted in front of the light source. To obtain highest quality measurement, light source, sample, and camera are aligned. Contact angles are determined using ImageJ@TM software. **Fig. A8.1(b)** shows contact angle of a water droplet (right) and epoxy droplet (left) on an FeNi MANC surface.

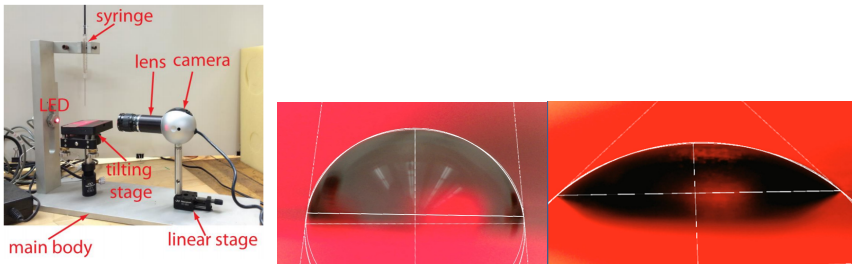

(a) (b)

Fig. A8.1: (a) apparatus built to measure the contact angle of a liquid droplet on a MANC sample to study surface energy; (b) contact angle of a water droplet (right) and epoxy droplet (left) on an FeNi MANC surface.

In this work we made important observations that will be detailed in a manuscript to be submitted. Important to the project is the determination that the epoxy contact angle is a strong function of the pre-applied strain in strain annealed (and re-annealed) FeNi based MANCs illustrated in **Fig. A8.2(a)** and that the epoxy wetting is anisotropic in strain annealed samples of **Fig. A8.2(b).**

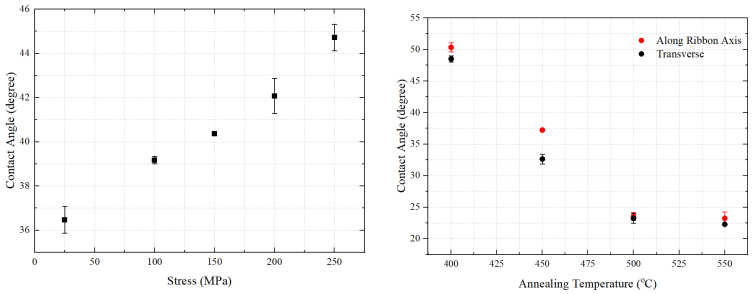

(a) (b)

Fig. A8.2: (a) illustrates the epoxy contact angle of a $(Fe_{70}Ni_{30})_{80}Nb_4B_{14}Si_2$ alloy strain annealed at 450 °C and (b) anisotropic wetting observed at lower strain annealing temperatures.

Appendix 9: Mechanical Properties: AMRs & MANCs.

Subtask 2.2.1 – Perform Tensile, Nanoindentation, and Bend Testing.

a. Tensile Tests: of CMU's FeNi80 alloy were used to determine stress-strain response, Young's Modulus (E) and Ultimate Tensile Strength (UTS). Measurements were performed on an Instron Model 4469 machine. Batch 1 ribbon, planar flow cast at 16.4 μm thickness, had undesirable edge roughness. Materials with large edge roughness exhibit lower material strength. Batch 2 ribbon had better edge quality. Smoother edges reflect ribbon samples from the middle of a casting batch, where nozzle pressure is better controlled. Batch 2 had an average thickness of 19.8 μm, that was more uniform across the ribbon width. **Fig. A9.1** shows an optical microscope observations of Batch 1 & 2 ribbon edges.

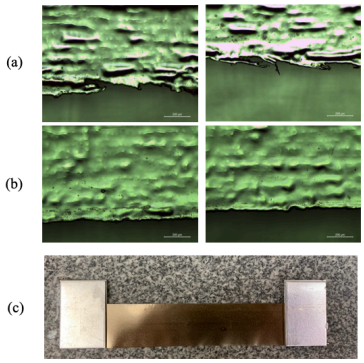

Fig. A9.1: Edge of ribbon in (a) Batch 1 and (b) Batch 2 (with 200 μm scale bar shown) and (c) full tensile test specimen attached to grip tabs by thermoset epoxy.

As-cast (AC) tensile specimens were cut to length and air annealed 15 min. at 440 °C. Room temperature curing epoxy was applied to ribbon ends and placed between sheet metal tabs (**Fig. A9.1**). The assembly prevents grip serrations from fracturing the ribbon when tightened. Batch 1 & 2 specimens (100 mm gauge length) were tested to failure monitored at 66,000 frames/s (15.2 μs between frames) with a high-speed camera (**Fig. A9.2**). Ribbon brittle fracture locations were observed in high-speed photography. Specimens failing away from the grips, were included in a failure stress population to obtain Weibull statistics. 26/27 samples failed away from the grips, indicating negligible grip stress concentration.

A majority of observations showed edge crack initiation. In Batch 1, all ribbons failed at an edge with larger roughness. In Batch 2, failures occurred on both sides. In only 6 cases did a surface flaw in the middle of the ribbon constitute the critical flaw, thus edge flaws generally limit ribbon strength. Specimens exhibit different crack propagation. **Fig. A9.2** shows failure modes I, II, and III. In each, the 1st image shows incipient propagation, the 2nd is at 75 μs (5 frames later). In failure mode I, **Fig. A9.2(a)**, crack branching is observed in a fanlike pattern. In mode II, **Fig. A9.2(b),** a primary crack dominates, with a few small branches. In mode III, **Fig. A9.2(c),** a crack originates in the strip center suggesting the critical flaw to be a surface defect. Specimens failing in mode I had a lower UTS than those failing in modes II & III.

Specimens with the lowest UTS (largest fatal flaw size) failed with mode I crack propagation, exhibiting many more cracks than modes II and III. Specimens storing less strain energy immediately before failure (lower UTS mode I failures) dissipate more energy in creating of many cracks than do specimens which sustain more strain energy at failure.

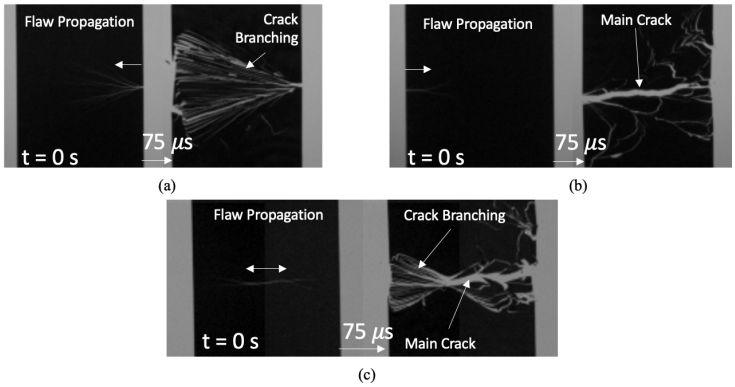

Fig. A9.2: Ribbon failure modes I (a), II (b), and III (c) near initiation and after 75 μs.

The difference in branching pattern could be due to both flaw size and a difference in crack tip shape. Specimens in Batch 2 (which fail in mode I) tend to have sharper crack tips impacting the propagation pattern. Mode I crack branching starts close to the ribbon edge. No matter the failure mode, higher quality ribbon surface and edges leads to higher UTS. Extension of the PFC process adding a polymer edge coating could improve edge quality.

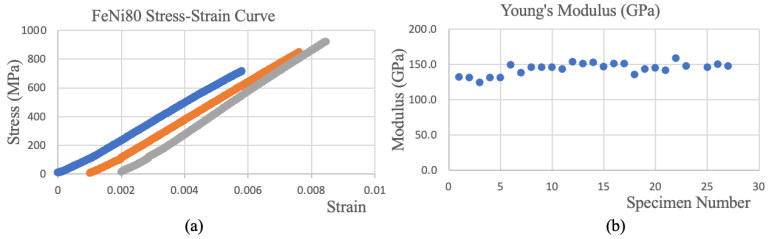

Fig. A9.3: (a) Tensile test stress vs strain results from three selected tests from Batch 2. Curves are shifted by 0.001 strain for clarity. (b) Youngs Modulus results for Batch 2 tensile tests.

Fig. A9.3a shows the stress-strain behavior of three tensile tests from Batch 2, shifted on the strain axis for clarity. These curves reveal elastic behavior until brittle failure, with no plastic deformation. Young's Modulus data obtained from tensile tests is shown in **Fig. A9.3b**, where the average result is 144 GPa with a standard deviation of 8.5 GPa.

Fig. A9.4 shows Weibull distributions of UTS for the FeNi80 alloy after the flash anneal described above, divided into Batches 1 and 2, from which 11 and 27 specimens, respectively, were tested. The Weibull modulus (*m*) describes repeatability of UTS. A larger number indicates a larger slope and more repeatable result. The ordinate value of 0 corresponds with the characteristic strength (σ_0) on the abscissa, where 63% of the failures occur at a lesser strength. The distributions for Batches 1 and 2 show *m* values of 2.869 and 3.814 and σ_0 values of 456 MPa and 1004 MPa, respectively. Lower σ_0 and *m* corresponds to larger edge roughness of Batch 1 ribbons demonstrating the importance of high-quality ribbon edges in stress-sensitive applications. Larger flaws in Batch 1 cause the distribution to be shifted to the left of the higher σ_0 Batch 2. Each ribbon in Batch 1 failed in mode I. This

agrees with findings from Batch II, where all ribbons exhibiting failure mode I failed at lower UTS values. These results correlate lower UTS values and larger flaw sizes in failure mode II.

Similar tensile testing conducted by Neilson et al. [1] on $Ni_{30}Ta_{35}Co_{30}Nb_5$ AMR reported a comparable *m* value of 3.2. Neilson reported a larger σ_0 value of 1.2 GPa for tensile tests and showed additional Weibull distributions for bend-over-mandrel tests. Bend-over-mandrel tests resulted in higher σ_0 and *m* values, due to a smaller ribbon length over which a high stress is applied. We expect σ_0 and *m* to similarly increase for alloys subjected to these tests. Although data points on the Batch 2 line reflect different modes, their slopes are not substantially different. This suggests incipient flaws cause brittle failure and with no substantial difference in failure mechanism. After initial crack extension, associated with measured UTS, dynamics of elastic energy dissipation may lead to different failure mode signatures observed.

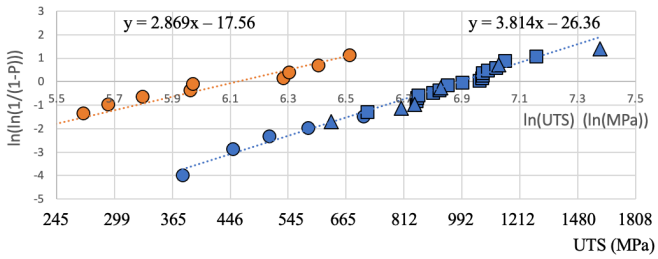

Fig. A9.4: Weibull distribution for Batch 1 (orange) and 2 (blue). Batch 2 is separated into failure mode by shape. Failure modes 1, 2, and 3 are denoted by circles, squares, and triangles, respectively.

b. Nanoindentation

Because of small ribbon thickness, nanoindentation requires specimens to be mounted on edge so as to indent on the ribbon edge. The ribbon specimen was thus encapsulated in a thermoset resin and its surface polished, as shown in **Fig. A9.5**. **Fig. A9.5b** shows loading and unloading curve from a typical nanoindentation test. 15 indentations were performed using a Berkovich tip up to a load of 1000 μN. The load range from 50% to 95% was used in fits of Young's Modulus and Hardness. The average Young's Modulus and Hardness were 130 GPa and 11.4 GPa, respectively. This Young's Modulus is 9% lower than that determined from tensile testing in good agreement to the limits of accuracy of nanoindentation.

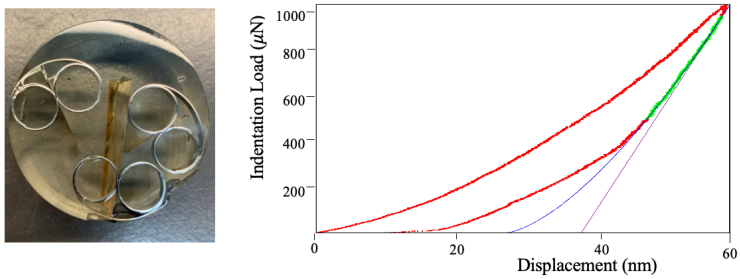

Fig. A9.5: (a) Ribbon specimens held vertically by epoxy for nanoindentation tests. Loading and unloading curve from nanoindentation experiment. (b) Region used for curve fitting is shown in green

c. Bend Tests

A common method to observe the brittle failure of traditional MANC alloys such as FINEMET is with bend tests. **Fig. A9.6** shows bend tests and the smallest possible radius prior to brittle failure in annealed ribbons, where FINEMET, **Fig. A9.6b**, fails at a larger radius than FeNi80, **Fig. A9.6a**. **Fig. A9.6c** shows FeNi80 ribbon after brittle failure in the AC (top), strained annealed (SA, middle), and strain annealed-reannealed (SA-RA, bottom) states. FINEMET is known to shatter into small pieces after annealing and bending, FeNi80 is holds a crease in both AC and SA states. After annealing for 15 min., SA-RA the FeNi80 fails in a single clean break upon being bent to a radius smaller than FINEMET.

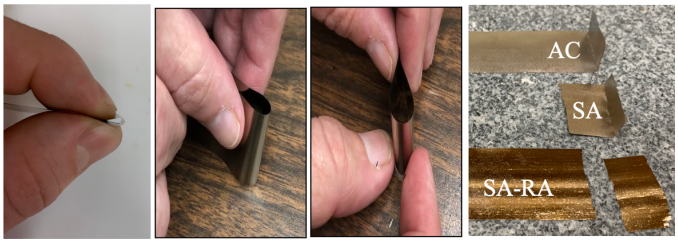

Fig. A9.6: Bend test for (a) FeNi80 after Strain Anneal/Reanneal (SA-RA) and (b) FINEMET after annealing showing smallest radius. (c) FeNi80 after ribbon creasing: AC (top), SA (middle), ACA (bottom).

Subtask 2.2.2 – Measure Densities of AMR and MANCs. Measure Properties.

a. Density Tests

Parsons [2] describes a method for predicting mass density of an amorphous or nanocrystalline alloy. Applying Parsons' regression function to the FeNi80 MANC alloy,

$$\rho = 7.751 + 0.010C^{Co} + 0.010C^{Ni} + 0.027C^{Nb} + 0.017C^{Cu} \\ -0.020C^{B} - 0.039C^{Si} - 0.032C^{P} \quad (1)$$

where C^i is the at.% content of element *i*. This model claims a fitting error of ±1% and results in a predicted density for the FeNi80 alloy in this study of 7741 kg/m^3.

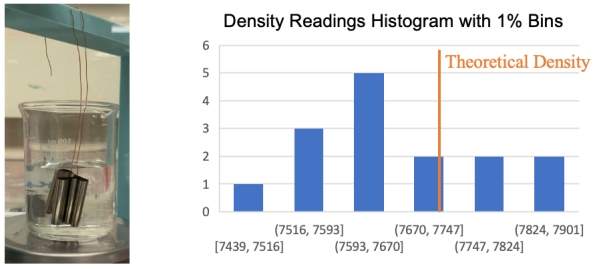

Fig. A9.7: (a) Wet mass measurement of bundled MANC ribbon suspended in water for density experiment. (b) Distribution of density measurements displayed in bins with width of 1% of the theoretical density value.

To corroborate this estimate, an Archimedean water displacement density method was used. AC ribbon specimens were bundled and air annealed. Ribbon specimen mass was first recorded, followed by wet mass measurement. In wet mass measurement, the balance is first

zeroed with a beaker of distilled water, the specimen attached to a wire, suspended and fully submerged in water, (**Fig. A9.7a)**. The mass of the submerged specimen is recorded as the wet mass, (mass of displaced water). The specimen density (**Fig. A9.7a**) is calculated using:

$$\rho = SG\rho_{H_2O} = \frac{m_{dry}}{m_{wet}}\rho_{H_2O} \quad (2)$$

with ρ, the density and m_{dry} and m_{wet} the wet and dry mass, respectively. Results (**Fig. A9.7b**) are depicted as a histogram with bin widths equal to 1% of theoretical density.

AMR and MANC ribbon density is difficult to measure due high surface area to mass ratio. The method employed relies on sufficient wetting of the ribbon surface with water used in the displacement experiment. Attention was paid to validating surface wetting to ensure no bubbles were brought beneath the water/ribbon surface. A theoretical density value is slightly larger than the density reading distribution centroid. The main source of measurement inaccuracy is the potential for micro-bubbles to adhere to the ribbon during its submersion in the water. If bubbles too small to be detected are present on the ribbon surface during the m_{wet} experiment, the density recorded will be lower than the value given by Eqn 2.

Subtask 2.2.3 – Initiate Rolling Studies of FeNi MANCs.

Rolling studies were not performed because sufficient reduction in ribbon thickness was achieved by adjusting the PFC process. Subsequent strain annealing was also determined to provide sufficient ribbon thinning. Ribbon thinning reduces eddy current losses, but reducing thicknesses below ~20 μm results in diminishing returns since ribbon surface roughness becoming significant and reducing achievable packing factor in a tape-wound core.

Subtask 2.2.4 – Develop FEA Mechanical Properties model of HSM rotor.

a. Mechanical Stress Modeling: We modeled and measured stresses in the flux-switching permanent magnet motor (FSWPMM) [3] rotor. These depend on residual stresses in manufacturing, rotational frequency, ω, and geometry. Given strength values, we assess whether a FSWPMM can sustain such stresses when delivering power at the level expected from electromagnetic modeling. We first summarize the manufacturing process.

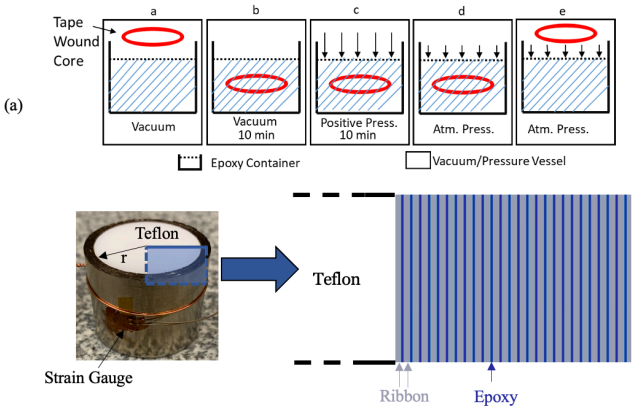

Fig. A9.8: (a) Vacuum pressure impregnation (VPI) process schematic. (b) Experimental tape-wound core with Teflon insert and applied strain gauge used to test impregnation and curing stress predicted by model. (c) Detail view of geometry used in axisymmetric FEA model for stress due to epoxy impregnation and curing

Epoxy impregnation increases tape wound core (TWC) strength in transformers and inductors. Epoxy impregnation and curing is important in HSM applications for to strengthen the TWC for waterjet cutting and motor operation. In vacuum pressure impregnation (VPI), a soft magnetic core is wound into a toroid is placed in vacuum to remove air from between layers, **Fig. A9.8a**. While under vacuum, the core is submerged into a liquid epoxy bath, **Fig. A9.8b**. A positive pressure is applied as in **Fig. A9.8c**, forces epoxy between ribbon layers. At atmospheric pressure, **Fig. A9.8d**, the core is removed from the bath, **Fig. A9.8e**. The epoxy-impregnated tape-wound core is cured in air at 160 °C, causing the epoxy to shrink [4].

While impregnation improves TWC strength by layer bonding, it degrades magnetic performance (in a magnetostrictive material) because the cure produces ribbon stress. Magnetoelastic coupling results in a magnetic permeability, coercivity, and energy loss per cycle dependence on stress state [5]. In transformer and inductor TWCs the stress state of stress is not as important for magnetic properties. The magnetic performance is measured before and after VPI and curing, but stress state is rarely documented. In new TWC high speed motor (HSM) applications the stress state is a critical design consideration. When the rotor of an electric motor rotates, its centrifugal force produces internal stresses that increase as rotational speed and rotor radius increase. Because thin MANCs are attractive for HSM applications due to low eddy current losses, rotational stresses are expected to be a design constraint from both a mechanical and magnetic perspective. Mechanically, the motor performs as a flywheel with maximum sustainable rotational frequency ω before rupture. High ω also alters the rotor's magnetic performance as emphasized previously.

To understand TWC rotor constraints, processing-induced and operational stresses must be modeled. Toroidal ribbon winding causes bending stress. Impregnation and curing induce circumferential stress, σ_θ. In operation, the rotor's rotational stress is significant. Here we discuss stresses due to epoxy solidification and contraction in TWCs and rotational stresses induced on the MANC/epoxy composite body. Literature [6] TWC stress [6], does not address epoxy contraction stress in impregnated TWCs. Ling [7] measured epoxy impregnation and curing stress at 3 points in a TWC, but did not model stress through the composite body or investigate impact of geometric and mechanical property changes. The effect of rotation on a toroidal body's stress state is known [8], but composite body stress (epoxy and MANC layered TWC) is more complex. Both are explored to understand TWC stress and relevant trends.

b. Model for stress induced by epoxy impregnation and curing

A wound toroidal core after being impregnated by the liquid epoxy is approximated by concentric ribbon rings of separated by epoxy layers, **Fig. A9.8b** and **c**. In the VPI process, a Teflon insert is placed inside the toroid to help the core hold its shape, the outer diameter is secured by wire to prevent the core from unwinding. Elastic material properties for MANC, epoxy, and Teflon are included in the model. Teflon properties are documented by the manufacturer and the MANC properties discussed in **Subtask 2.2.1**. The epoxy manufacturer provides neither Young's Modulus nor volume change upon curing data.

To determine the Young's Modulus, small tensile test specimens were created using a scaled tensile specimen based on the ASTM E8 standard. The specimen dimensions are shown in **Fig. A9.9a**. **Fig. A9.9c** shows representative tensile test stress-strain result for the VonRoll 74030 thermoset epoxy resin used in here as measured by a tensile test machine using a smaller load cell more appropriate to for smaller polymer specimens. From this data, the strain range from 1.5% to 2.5% was selected for determining the Young's Modulus of 1.15 MPa, with a UTS of 74 MPa.

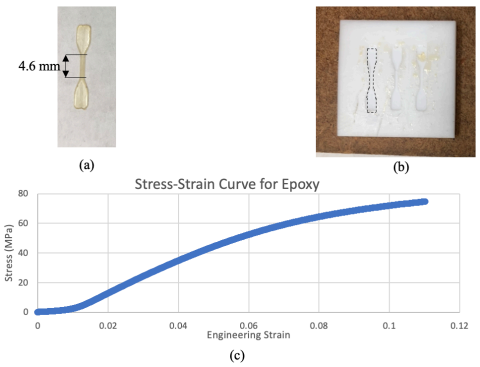

Fig. A0.9: Epoxy tensile test specimen (a), mold used to create specimens (b). Epoxy stress-strain curve (c)

An epoxy curing stress model \considers the volume change due to the epoxy phase change. Epoxy data sheets report specific gravity (from which density is calculated, Eqn 2) of the liquid phase. Thus, only solid phase density is needed to calculate the volume change. The solid phase density was fdetermined by the method in **Section 1d, Subtask 2.2.2**. Eqn 3 is used to calculate volume contraction. An average of 5 specimens volume contraction was 4.6%. Material properties used in the epoxy contraction model are shown in **Table A9.1**.

$$\frac{\Delta V}{V} = \frac{V_2 - V_1}{V_2} = \frac{\frac{m}{\rho_2} - \frac{m}{\rho_1}}{\frac{m}{\rho_1}} = \frac{\frac{1}{\rho_2} - \frac{1}{\rho_1}}{\frac{1}{\rho_1}} \quad (3)$$

Table A9.1: Material properties used in epoxy curing model

Variable	Value	Description
E_e	1.15 GPa	Epoxy Modulus
E_r	144 GPa	Ribbon Modulus
E_t	2 GPa	Teflon Insert Modulus
υ	0.3	Poisson's Ratio for all Materials
$\alpha_{e,\,cure}$	0.045	Epoxy Curing Contraction Coefficient
α_e	5.0E-5	Epoxy Solid Phase CTE
α_r	1.1E-5	Ribbon CTE
α_t	1.2E-4	Teflon CTE
t_e	5 μm	Epoxy Layer Thickness
t_r	20 μm	Ribbon Layer Thickness

An epoxy impregnation curing model was developed in ANSYS WB 2021 R2 using an axisymmetric TWC, approximating ribbon & epoxy windings as concentric rings. The model was used for a small test core to optimize computational speed and subsequently applied to motor TWC size. A geometry of 25 mm diameter Teflon, 29 mm outer core diameter, a 16 μm ribbon layer thickness and a 6 μm epoxy thickness was used. Epoxy thickness was estimated by unwinding an impregnated TWC combining and calculating the MANC core packing factor.

Epoxy curing was modeled with 3 time steps. (1) a temperature load applied to the assembly increases T from 22 to 160 °C, representing ramping the impregnated assembly in a preheated oven to the epoxy cure T. The liquid epoxy has a negligible Young's Modulus and Teflon expands more than ribbon layers (due to a higher CTE), causing ribbon tension and Teflon compression. Due to ribbon roughness, the space between the ribbons does not change significantly. (2) simulates epoxy solidification, applying a T load of -1 °C to the assembly with a positive CTE present only in the epoxy. Young's Modulus of the epoxy increases to that of the solid phase. Viscoelasticity is ignored. This step introduces a complex stress state altered by the final load step. (3) a final time step reduces assembly T to 22 °C, where Teflon contracts by an amount sufficient to separate it from the inner core surface.

After 3 time steps, the epoxy curing model stress distribution is shown in **Fig. A9.10a** in blue. The θ direction is circumferential (ribbon lengthwise) direction. The figure shows epoxy curing results in θ tension in epoxy layers that does not vary greatly between inner (r_1) and outer(r_2) radii. Tension is present because ribbon layers have high stiffness and resist epoxy contraction. Ribbon stress varies from tension at r_1 to compression at r_2. This stress variation is only present in toroids of sufficient layer count, as toroids with ~10 layers exhibit only compressive stress due to the epoxy compressing the ribbon towards the toroid center. With many more layers the toroid contracts toward $r \approx \sqrt{r_1 r_2}$, and tension at r_1 and compression at r_2. Curves for epoxy and ribbon stress are individually labeled in **Fig. A9.10a**.

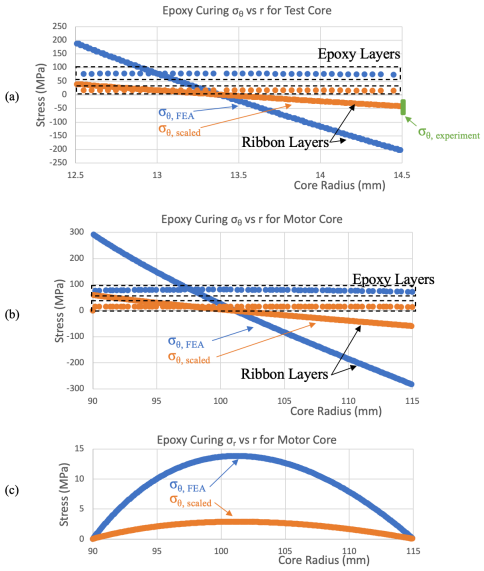

Fig. A9.10: Experimental impregnation stress result (green bar) compared with FEA model stress distribution (blue) and FEA model scaled to match experimental results (orange). Stress in ribbon and epoxy regions are labeled. Results shown for 25 mm ID, 29mm OD core. Model prediction of (b) σ_θ and (c) σ_r stress vs core radius due to epoxy impregnation.. Results shown for 180 mm ID, 230 mm OD core.

The magnitude of the stress predicted by this model is large relative to epoxy yield stresses (UTS ~74 MPa) and ribbon (characteristic strength of ~1.0 GPa). However, the model

produces stress values higher than in the real curing process because the model assumes immediate epoxy solidification. Transient in contrast to instantaneous epoxy solidification requires considering viscoelastic relaxation of the mechanical stress. To validate, strain measurements were conducted on a TWC of the model geometry. **Fig. A9.10a** shows this TWC, including a strain gauge mounted to the outer ribbon surface, facing the θ direction. Bonding with high-temperature adhesive and measuring strain before and after impregnation/curing, the outer surface curing stress ($\sigma_{\theta,\ exp}$) was determined. **Fig. A9.10a** compares a circumferential stress profile FEA model ($\sigma_{\theta,\ FEA}$) with $\sigma_{\theta,\ exp}$. The experimental stress is used to scale the stress distribution to relate $\sigma_{\theta,\ FEA}$ to $\sigma_{\theta,\ exp}$. These results show $\sigma_{\theta,\ exp} = 0.2\sigma_{\theta,\ FEA}$. σ_{θ}^{exp}

Fig. A9.10b and **c** show results of the model of **Fig. A9.10a**, but with the rotor geometry of this project. Both σ_θ and σ_r are shown for the result of the FEA model, as well as scaled stress values. Values use the scale same factor as in **Fig. A9.10a**, as informed by stress experiments performed on the smaller TWC. We used this scaling method (by a factor of 0.2) as a method of accounting for the viscoelastic stress relaxation. Further refinement of this approach may be warranted as stresses may depend on geometry and material properties.

c. Model for stress induced by rotation of TWC in motor application

Because the FWPMM motor is designed to take advantage of the high-frequency switching of MANCs, a high rotational speed of the rotor is expected for a design pursuing high power density. A series of simulations of increasing geometrical complexity is have been performed to account for the motor geometry. These are labeled as Cases I-IV as described in **Table A9.2**, and each analysis uses r_1 and r_2 values of 90 and 115 mm, respectively.

Table A9.2: Rotational stress analysis assumptions for Cases I-IV

Case	Geometry	Layers	Modeling Method	Effect on σ_θ relative to Case I	Effect on σ_r relative to Case I
I	Simple Toroid	Single Elastically Isotropic Material	Analytical	-	-
II	Simple Toroid	Layered Materials	FEA	↑ 21%	↓ 10%
III	True Geometry	Single Elastically Isotropic Material	FEA	↑ 26%	↑ 35%
IV	True Geometry	Layered Materials	Superposition of I, II and III with stress concentrator	↑ 47%	↑ 25%

Beginning with Case I for a homogeneous body, increasing the rotational speed increases mechanical stress in the rotor by the square of the rotational speed (ω), as given in equations 4 and 5 [8], which give σ_θ and σ_r vs radius (r) for a toroid with uniform density (ρ).

$$\sigma_\theta = \rho\omega^2 \left(\frac{3+\nu}{8}\right)\left(r_i^2 + r_o^2 + \frac{r_i^2 r_o^2}{r^2} - r^2\right) \quad (4)$$

$$\sigma_r = \rho\omega^2 \left(\frac{3+\nu}{8}\right)\left(\mathrm{r_i^2} + \mathrm{r_o^2} + \frac{\mathrm{r_i^2 r_o^2}}{r^2} - \frac{1+3\nu}{3+\nu} r^2\right) \quad (5)$$

This equation is used as a lower bound for stress in a TWC rotor and to calculate Case I stress distribution. Because the rotor consists of ribbon and epoxy layers, the stresses (4&5) consider a density determined by a rule of mixtures. Case I results give stress trends, with two assumptions made model which differ in a rotor made from a TWC: (1) the rotor is a composite of ribbon and epoxy layers, rather than a homogeneous material; (2) the rotor is not a simple toroid with axisymmetric geometry. Modeling a 3D rotor with all layers meshed to capture both effects is impractical, so the layered and 3D nature of the rotor were considered separately.

Table A9.3: Material properties used in rotational stress models

Variable	Value	Description
E_e	1.15 GPa	Epoxy Young's Modulus
E_r	144 GPa	Ribbon Young's Modulus
$E_{combined}$	136 GPa	Rule of Mixtures Modulus for Case I
υ	0.3	Poisson's Ratio
ρ_e	1170 kg/m³	Epoxy Mass Density
ρ_r	7741 kg/m³	Ribbon Mass Density
$\rho_{combined}$	6427 kg/m³	Rule of Mixtures Density for Case I
t_e	5 μm	Epoxy Layer Thickness
t_r	20 μm	Ribbon Layer Thickness

Case II models the layered composite nature of the rotor using an axisymmetric model in FEA like that discussed for epoxy impregnation and curing processes without the Teflon insert. Material properties used in the analysis of Cases I and II are shown in **Table A9.3**. **Fig. A9.11** shows the σ_θ and σ_r distributions for Cases I and II for a rotational speed of 15,000 RPM. Case I exhibits a maximum σ_θ of ~20% of the ribbon characteristic strength at the r_1, which decreases toward the r_2. Because r_1 and r_2 are unsupported, σ_r is zero at these surfaces, but becomes tensile in the interior. When Case II is modeled, epoxy layers take on far lower σ_θ because their Young's Modulus is much lower. The stress, borne by the ribbon layers, yields a σ_θ increase of ~20% due to the 20% reduction in area responsible for bearing this stress. A reduction in σ_r is observed in Case II due to low epoxy Young's Modulus and continuity of σ_r with increasing radius. **Table A9.2** summarizes the effects on σ_θ and σ_r in the last two columns.

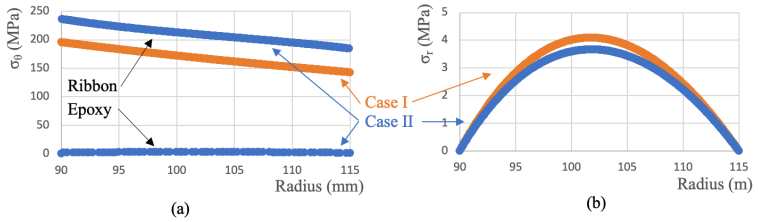

Fig. A9.11: Rotational stress distribution of σ_θ (a) and σ_r (b) for Case I and Case II

The true geometry (without epoxy) for Case III is shown (**Fig. A9.12**) labeling regions of interest. This model, built in ANSYS Workbench 2021 R2, applies a rotational load of 15 krpm, using material properties determined by a rule of mixtures. The TWC is 80% volume fraction ribbon and 20% epoxy. Young's Modulus and density are determined multiplying each property value by its volume fraction and summing over both materials. Like Case I, the modulus is isotropic. Case II captures effective isotropic response of the TWC.

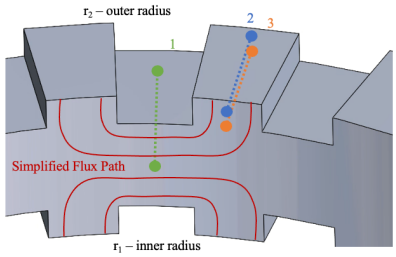

Fig. A9.12: Rotor zones used for Case III rotational stress trends. These zones are the middle of the flux return path (1), the middle of the rotor tooth (2), and the rotor tooth base (3).

Case III σ_θ and σ_r distributions are shown in **Fig. A9.13**. In **Fig. A9.12**, the curve labeled 1 is the middle of the flux return path, the curve labeled 2 is the middle of the rotor tooth, and the curve labeled 3 is the rotor tooth base. **Fig. A9.13** shows Case III results in σ_θ increase in regions 1&3 by a similar amount to Case II. Nearer to the rotor tip in region 2, σ_θ is significantly reduced. While Case II shows a decrease in σ_r, Case III, regions 1&3, show a small increase compared to Case I. Significant σ_r compression develops close to the rotor tip in region 2 of Case III. In all cases a maximum stress is found at $r = r_1$ for σ_θ and at $r \approx \sqrt{r_1 r_2}$ for σ_r.

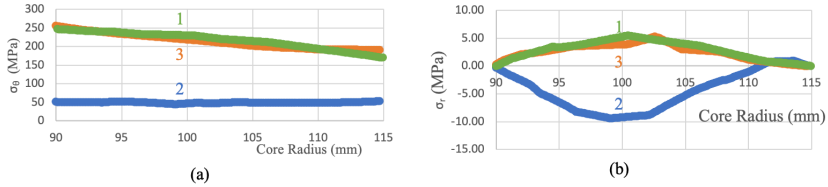

Fig. A9.13: Rotational stress distribution of (a) σ_θ and (b) σ_r from FEA for Case 3 with zones labeled. The labels 1, 2 and 3 are from the regions indicated in Fig.A9.12.

Rather than study stress concentration of a sharp internal corner at each rotor pole, we analyzed stress at these corners using well-known stress concentration values. To determine the corner radius after the waterjet cutting process, optical microscopy was employed, **Fig, A9.14**. 3 images were analyzed to determine the corner radius to be 0.42 mm. Using results from Kumagai [9], the stress concentration factor for each corner was calculated to be 2.9.

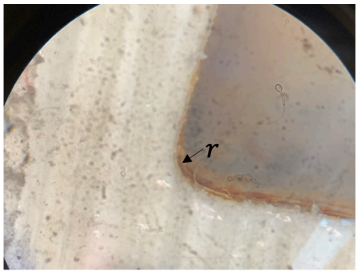

Fig. A9.14: Optical microscope view of inner corner of rotor tooth used to estimate corner radius.

The stress in a layered composite TWC rotor of **Fig. A9.12**, Case IV was inferred using Case I as a baseline. From Case I, Cases II and III result in a %change in maximum stresses. The % increases are added to infer the maximum rotor stress. This analysis is simpler because each case exhibits its maximum σ_θ and σ_r at nearly the same respective locations in the rotor.

Table A9.3: Stress increase when effects of Cases II and III are considered in conjunction with the rotor pole corner stress concentrator. Results are shown for rotor speed of 15,000 RPM

	σ_r	σ_θ
Case I Max Stress (MPa)	4	195
Case II Scaling Factor	-10.4%	20.8%
Case III Scaling Factor	35.3%	25.8%
Total (Case IV) Scaling Factor	25.0%	46.6%
Case IV Stress (MPa)	5	287
Stress Concentration Factor	1	2.9
Impregnation Stress (MPa)	5	115
Case IV r_1 Corner Stress (MPa)	10	1165
Case IV FoS	7.32	0.86
Revised Geometry Stress Concentration Factor	1	2
Revised r_1 Corner Stress (MPa)	10	803
Revised Geometry FoS	7.32	1.24

Table A9.3 shows maximum σ_θ and σ_r for Case I, and scaling factors (% increase in stress relative to Case I) due to Cases II and III, also shown graphically in **Fig. A9.15**. Case III scaling factors for σ_θ and σ_r were from the zone 3. After stresses are scaled due to the effects of Cases II and III, the stress due to epoxy impregnation was added. The resultant σ_θ was scaled by the stress concentrator previously determined because the stresses flowing in the θ direction flow around the corner feature. The σ_r stress, however, does not need to flow around this feature, and thus does not give stress concentration. The Factor of Safety (FOS) calculation uses epoxy failure stress of 74 MPa for σ_r and ribbon failure stress of 1 GPa for σ_θ^{char}, the characteristic strength from prior experiments. This provides an FOS reference point.

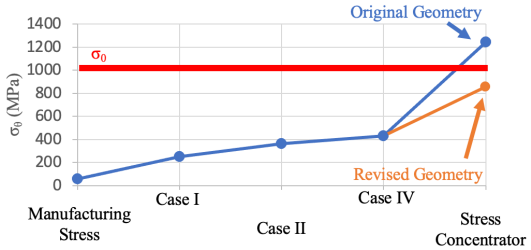

Fig. A9.15: Maximum σ_θ stress in TWC rotor when different assumptions in Cases I, II, and III are considered (Case IV is I, II, and III combined).

Table A9.3 analyzes Case IV FOS, the rotor (as currently designed) will have σ_θ tensile stress exceeding σ_o of the ribbon at each internal rotor pole corner at r_1. The high stress concentration factor of 2.9 rsults from the small radius of these internal corners. This corner radius need not be so small for magnetic performance of the motor. The rotor can be redesigned with these corners having a radius of 2.7 mm to achieve a stress concentration factor of 2 [9]. σ_θ result and associated FoS for this improved design are shown in **Table A9.3**.

d. Conclusion/Recommendations

Because of ribbon brittleness and high stresses in the rotor, we added a feature supporting r_2 to the hub, connecting the rotor and motor shaft. A concept design is shown in **Fig. A9.16**. This feature constrains ribbon layers and serves as a failsafe if ribbon fracture were to occur. Further analysis was used to optimize this component considering improvements to the Weibell analysis and FOS with epoxy impregnated ribbon stacks.

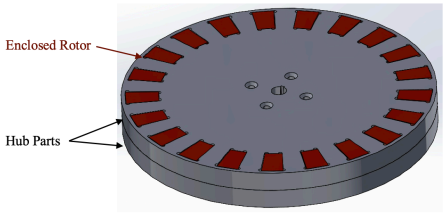

Fig. A9.16: Rotor shown in red enclosed by two hub components

The point of failure predicated by the above analysis occupies a relatively small region when compared with the rotor volume. Since the failure of MANC ribbons is dominated by the flaw size, it is worth investigating the statistical likelihood of a critical flaw existing at this geometrically small local stress concentration. Tensile tests presented here study ribbon samples with edge surface finish after PFC, rather than after waterjet cutting. In actual use, the stress concentrating corner would result from waterjet cutting, with a different surface finish. Extensions of this work require tensile test data for impregnated stacks of ribbon and epoxy in both full width and waterjet-cut configurations. Studying impregnated stacks will help determine whether epoxy layers prevent rapid crack propagation and improve toughness of the TWC composite through plastic deformation..

Since a σ_o benchmark was used in this assessment, this design philosophy is not conservative. However, the tensile test behavior of a composite TWC may be different than that of a single strip of MANC ribbon. Because the epoxy material fails at much larger strains than the ribbon, a stack of ribbons impregnated with epoxy may exhibit a more repeatable UTS. Additionally, the composite may exhibit plastic deformation after brittle failure (**Fig. A9.4**). Weibull statistics of the composite material structure are detailed in an accepted manuscript.

References

[1] H. J. Neilson *et al.*, "Weibull modulus of hardness, bend strength, and tensile strength of Ni-Ta-Co-X metallic glass ribbons," *Mater. Sci. Eng. A* **634**, 176–182, (2015). doi: 10.1016/j.msea.2015.03.006.

[2] R. Parsons *et al.*, "Prediction of density in amorphous and nanocrystalline soft magnetic alloys: A data mining approach," *J. Alloys Compd.* **859**, (2021). doi: 10.1016/j.jallcom.2020.157845.

[3] S. Simizu, P. R. Ohodnicki, and M. E. McHenry, "Metal Amorphous Nanocomposite Soft Magnetic Material-Enabled High Power Density, Rare Earth Free Rotational Machines," *IEEE Trans. Magn.* **54**, 1–5, (2018). doi: 10.1109/TMAG.2018.2794390.

[4] D. U. Shah and P. J. Schubel, "Evaluation of cure shrinkage measurement techniques for thermosetting resins," *Polym. Test.* **29**, 629–39, (2010). doi: 10.1016/j.polymertesting.2010.05.001.

[5] R. C. O'Handley, "Magnetic core loss and internal stress in metallic glasses," **206**, 206–08, 2008, doi: 10.1063/1.30586.

[6] W. Grimmond, A. J. Moses, and P. C. Y. Ling, "Dimensional factors affecting magnetic properties of wound cores," *Phys. Scr.*, vol. 40, no. 2, pp. 249–251, 1989, doi: 10.1088/0031-8949/40/2/017.

[7] P. C. Y. Ling, A. J. Moses, F. McQuade, W. Grimmond, and D. Fox, "Investigation of magnetic degradation of wound cores due to adhesive bonding," *J. Magn. Magn. Mat.* **112**, 77–80, (1992), doi: 10.1016/0304-8853(92)91117-C.

[8] S. Timoshenko, *Theory of Elasticity*, 2nd ed. McGrae-Hill Book Company, (1951).

[9] K. Kumagai, "The Stress Concentration Factor Produced by a Projection under Tensile Load," *Bull. JSME* **117**, 739–45, (1968).

Appendix 10: Oxide Properties of AMR and MANCs

As discussed in Appendix 9, ribbon flaws can result from surface structural variations, therefore it is important to understand the MANC ribbon surface roughness. Roughness reflects the passivating surfaces oxides shown in Figure A10.1. For this reason, analysis of MANC oxidation and surface roughness are reported in: J. Egbu, P. R. Ohodnicki, J. P. Baltrus, A. Talaat, R.F. Wright and M. E. McHenry; Analysis of Surface Roughness and Oxidation of FeNi-Based Metal Amorphous Nanocomposite Alloys. J. Alloys & Compounds **912**, 165155, (2022).

This thin passivation oxide, and its anisotropy derived from strain annealing is postulated to influence the epoxy wetting in the vacuum impregnation bonding of tape wound cores (**App. 8**). Epoxy wetting of MANCs was presented at the 2022 MMM/Intermag (Anaheim) and 2022 MMM (Minneapolis) conferences. Detailed studies will be reported in the CMU MSE Ph.d thesis of J. Egbu.

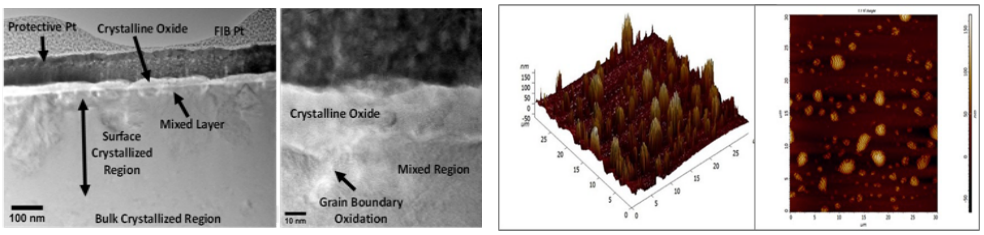

(a) (b)

Fig. A10.2: (a) Cross-sectional TEM Images of surface crystalline oxides on an FeNi-based MANC and (b) AFM determined surface roughness of the same.

Thickness and composition of surface oxides on FeNi-based AMR and MANC were determined by selected oxidation studies performed by annealing the AMR in air for different times and temperatures. FeNi-based AMRs have an Fe-rich surface oxide with amorphous structure, shown by TEM in **Fig. A10.1a**. AMR average surface oxide thickness was determined to be ~4 nm comprised mainly of Fe-oxide at the top surface followed by Nb, B, and Si oxides. Bulk resistivity of FeNi-based AMR was measured and reported as ~159 μΩ-cm. After a 30 min conventional annealing in air, the average surface oxide thickness increased to ~10 nm. We have also reported resistivity of 150-200 μΩ-cm in FeNi-based MANCS [1]

FeNi-based MANC surfaces were coated with epoxy resins by vacuum pressure impregnation. Improved epoxy wetting was observed by measuring the contact angle by sessile droplet method (App.8). Improved epoxy adhesion is observed with thicker oxide layers. Epoxy resins can be excellent electrical insulators but may show non-linear properties in high electrical fields. Electrical properties of epoxies indicate a volume resistivity of 2 x 10^{12} - 3 x 10^{14} ohm-cm and surface resistance of 2 x 10^{11} - 3 x 10^{12} ohm for cured epoxy. [2]

Resistivity reported for epoxy is significantly exceeds the 500 μΩ-cm of the milestone. Thus, resistivity of the coated laminates is much higher than in uncoated laminates. A recent IEEE report [2] shows a decreasing volume resistivity from 10^{14}-10^{10} ohm-cm as the electrical field increases to 10 kV/mm for SiC-filled epoxy resin under cryogenic temperature. Such behavior is of interest for the development of superconducting transmission cable. [3] While parent oxides provide sufficient interlayer isolation, epoxy impregnation also contributes to mechanical integrity of tape wound cores. MANC TEM was performed on FeCo Metglas AMRs. TEM analysis we observed:

(a) Featureless low magnification images are typical of an amorphous material.
(b) Electron diffraction patterns showed broad rings typical of amorphous materials. In addition there were 2 distinct rings indicating of local ordering.
(c) High resolution TEM (HRTEM) confirmed the existence of very small, sub-nanometer ordered clusters (embryos) typical in undercooled or frozen liquids**.**
The material was fully amorphous, rings reflect a passivating amorphous surface oxide.

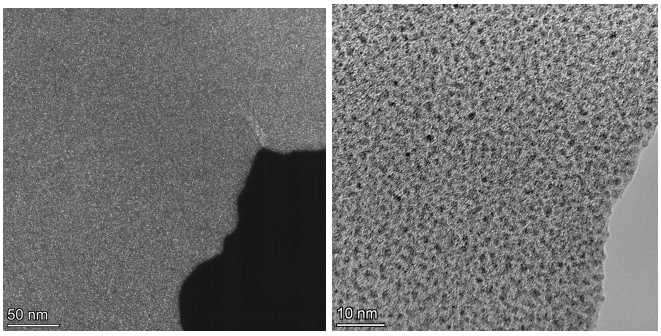

(a) (b)

Fig. A10.2: (a) dark field TEM image (135 kX) collected with an aperture over an amorphous electron diffraction pattern ring; (b) high resolution TEM (HRTEM, 580 kX) image showing uniformly distributed sub-embryonic clusters.

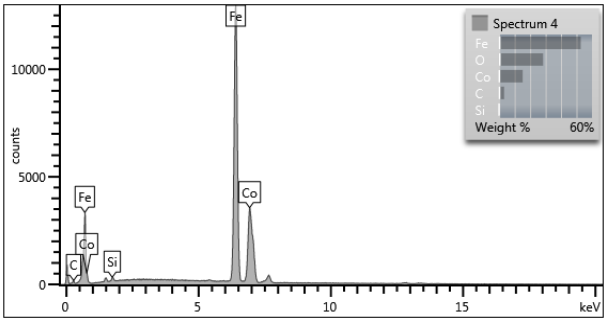

Fig. A10.3: EDAX composition results from an FeCo-based AMR materials showing Fe, Co & Si chemistry.

Fig. A10.3 shows EDAX results for FeCo-based AMR materials. Fe, Co and Si are observed in nominal ratios expected of the alloy chemistry. B is difficult to resolve with EDAX techniques.

1. Aronhime, N., Ohodnicki, P. & McHenry, M. E. Virtual bound states elements and their effects on magnetic and electrical properties of Fe-Ni based metal amorphous nanocomposites. Scr. Mater. 169, 9–13 (2019).
2. C. Pitt, B. Barth and B. Godard, "Electrical Properties of Epoxy Resins," in IRE Transactions on Component Parts, vol. 4, no. 4, pp. 110-113, December 1957, doi:10.1109/TCP.1957.1135915.
3. Z. Li, B. Du and T. Han, "Nonlinear Conductivity of SiC/Epoxy Resin Composites Dependent on Electric-Field at Cryogenic Temperature," 2020 IEEE International Conference on Applied Superconductivity and Electromagnetic Devices, 2020, pp. 1-2.

Appendix 11: FSWPM Motor Testing.

NCSU received parts from CMU for drive and loss decomposition testing. NCSU identified anomalies in the motor following shipping. The back EMF was measured and showed substantial torque imbalance in both magnitude and phase between stators. Previous tests at CMU had demonstrated much better back EMF matching so it was determined the motor was altered during shipping. In addition to the back EMF mismatch, mechanical 'thumping' was observed once per revolution and substantial cogging was evident.

To correct the aforementioned deficiencies the motor housing was realigned and the rotor end play was trimmed. Peak MMF imbalance was reduced from 18 to 5% and cogging significantly improved. 5% MMF mismatch is significantly worse than COTS radial flux motors, but further improvement was impeded by the error-prone manual motor assembly procedure. Note that the phase error of the relative stator angles is not adjustable, so there is no remedy for the several degrees of phase error. After adjustments it was judged that MMF matching could not be further improved and testing should proceed cautiously.

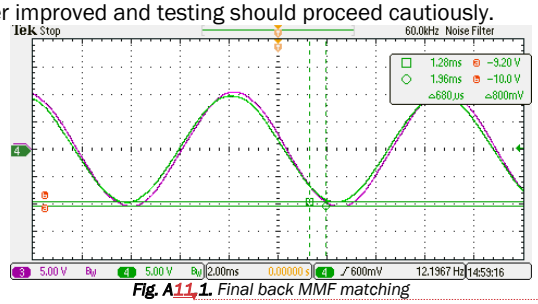

Fig. A11.1. Final back MMF matching

Further troubleshooting determined that 'knocking' was due to rotor instability on the shaft. The asymmetric magnetic forces were causing the rotor to rock back on the shaft through one mechanical cycle. Rotor instability also led to poor rotor face runout and varying of the gap. To remedy this, a new press-fit Al hub was designed and machined. This component engages the face of the rotor to provide better angular support. Additionally, torque is now transferred between rotor and Al support, then from Al support to the shaft instead of relying on the previous keyed connection. The new Al hub increased stiffness, reduced face runout, and eliminated rotor 'knocking' so testing could proceed (**Fig. A11.2**).

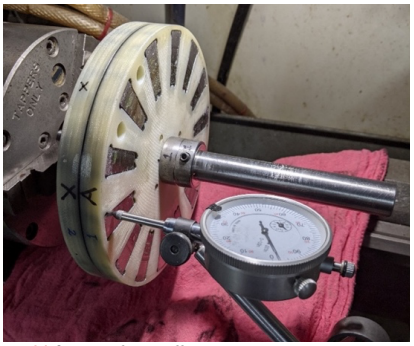

Fig. A11.2. Rotor face stiffness and runout measurements.

Deleted:

Deleted: x

Deleted: x

No-load back-drive testing was performed to determine core losses and check motor behavior at high RPM. Due to rotor instability, there was some difficulty controlling the driving machine so control was reverted to open-loop V/F control. In this test both it was necessary to separate iron and bearing losses.

A LUNA ODiSi fiber optic temperature interrogator was used to measure the temperature at the stator teeth (**Fig. A11.3**). This system allows measurement of the temperature at points along an optical fiber and is completely immune to the magnetic fields side the motor. So, it was possible to measure the temperatures of several stator teeth on each stator to verify that iron losses are uniform, which they were, and to separate iron loss from bearing losses. Iron losses for the metal amorphous nanocomposite material is extremely low, so it was still difficult to measure. In general, the iron loss was very similar to the bearing loss at any given RPM. At 1000 RPM the iron losses were only about 6W, and at 2500 RPM it scaled roughly linearly to 14W. It was not possible to test much above 2500RPM due to mechanical resonances developing in the setup. So, attempts were made to stabilize the motor for further testing.

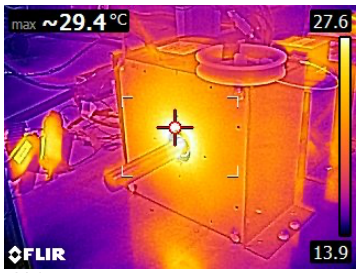

Fig. A11.3: *External temperature at 2500RPM operation.*

The original motor housing consisted of composite end plates supporting the bearings and stator with aluminum interconnect elements. This housing was easy to work on and allowed excellent access to the motor, but was not very rigid when mounted to the test stand. There was substantial change in rotor gap and bearing pre-load from attaching the motor to the stand. So,support plates were installed to support 3 sides of the motor to increase rigidity and allow mounting without unintentional change to motor gaps or bearing pre-load.

The rotor was statically balanced by K. Byerly at CMU. Initial testing showed the rotor balance was still inadequate, so dynamic balancing was performed locally at the maximum rated 6 kRPM. This confirmed the structural integrity of the rotor that consists of the MANC core and glass fiber composite housing and the 20 mm shaft, because it was the first time the motor was run at rated RPM.

The red circles (**Fig. A11.4**) are the original balancing holes drilled at CMU, and these additional 6 holes were required for dynamic balancing. Given the inhomogeneity of the fiberglass rotor hub and magnetic core material itself, it is recommended that future designs provide additional locations for balancing holes in locations designed specifically to preserve structural integrity of the rotor. Structural integrity was not a problem in this case but it is a design concern with higher speed motors and/or larger diameter rotors.

Fig. A11.4: Balancing holes drilled in the rotor housing. In addition to the original two static balance holes (red circle), four holes were added to achieve dynamic balance.

After improvements to the rotor hub, motor housing, and dynamic balancing of the motor drive tests were restarted (**Fig.A11.5)**. At low speed there are two anomalies related to the motor build. First, at low speed the current zero crossing there is an inflection point due to the phase mismatch between stators. Secondly, at low speed there is also variation in the peak current at each electrical cycle due to peak MMF mismatch.

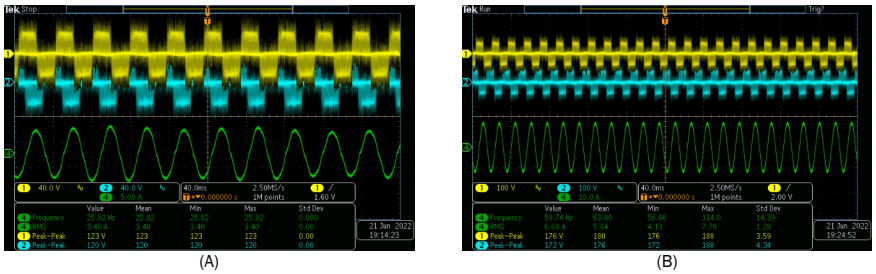

(A) (B)

Fig. A11.5*. Drive waveforms at low RPM (A) and high RPM (B).*

At high speed these anomalies are less evident, and in general the mechanical non-idealities are acceptable until the inception of resonance in the test setup. 3.5 kRPM was achieved before testing was ceased due to strong resonance between the rotor and test setup.

In summary, after overcoming various mechanical and test setup hurdles, it was observed that the core loss in the MANC material is extremely low. In the tests performed the core loss is so small that it is difficult to distinguish from the bearing loss without specialized instrumentation. Looking toward the future of high speed axial flux machines the primary difficulties pertain to the mechanical processing of MANC cores and the mechanical construction of the motors. Towards commercialization of high-speed axial flux motors using MANC materials, there is some exploration to be done in the processing of the MANC material into dimensionally consistent rotors and stators.

Appendix 12: Loss Metrics, Materials Benchmarking and Potential for Commercialization

Metglas served as our industrial partner with their role in the program to demonstrate commercial levels of production of CMU novel alloys and show the potential for commercial motor production. Casting of the FeNi-80 and FeNi-85 alloys were shown at up to 2" widths and thicknesses of 15-25 μm. An experimental batch casting machine was used to cast alloys. This 20 kg batch casting machine demonstrates the feasibility of scaling up to larger volumes.

Prototype toroidal cores were produced from the FeNi-80 alloy and from a commercial FeCo amorphous alloy. The FeCo alloy has the tradename Metglas2605CO and has the highest saturation induction of any amorphous alloy available today at 1.8 T. The procedure to make these toroids was to first anneal foils in bulk form and then co-wind them with a thin Mylar layer to insulate the laminations. This processing does require the foils to be mechanically ductile during the co-winding process. This is not possible with conventional Finemet type nanocrystalline alloys. The cores were then vacuum impregnated with an epoxy for structural rigidity. The final core is shown in **Fig. A12.1(a)**.

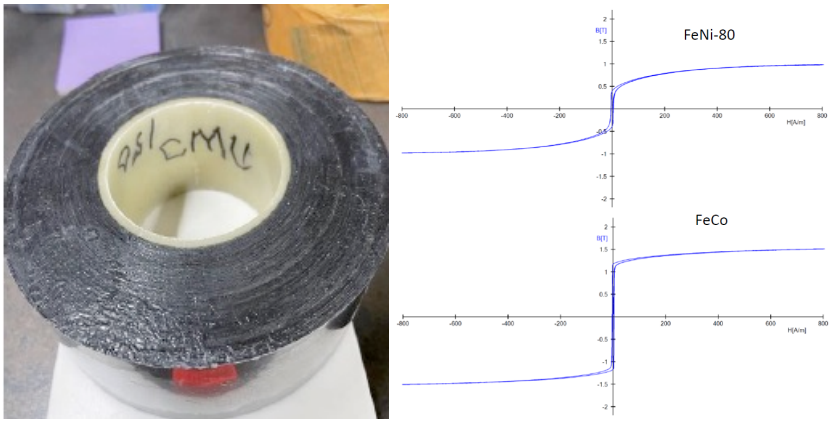

(a) (b)

Fig. A12. 1. (a) Toroidal core co-wound with a Mylar and epoxy bonded; (b) BH loops for FeNi and FeCo toroids.

FeNi and FeCo cores were measured for magnetic properties. **Fig. A12.1(b)** shows BH loops of each core. After co-winding and epoxy impregnation magnetic properties deteriorate slightly and cores are more difficult to drive to the saturation but still show very low coercivities.

Metglas has partnered with **Flux Dynamics**, a third party motor startup company. Their concept is to produce low cost amorphous stators coupled with ferrite rotors to produce highly efficient motors. The target market is replacing high volume induction motors. Metglas fabricated with FeNi and FeCo toroids and sent them to Flux Dynamics to convert them into stators. The initial prototypes were made by conventional cutting and grinding methods. Flux Dynamics also performed the testing of stators on their motor test stand. **Fig. A11.2(a)** shows that stator after the slots were cut.

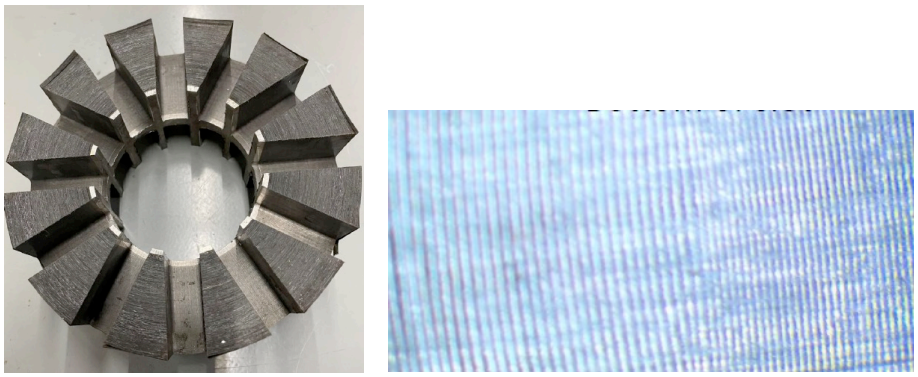

(a) (b)

Fig. A12.2. (a) Stator after slot machining; (b) optical image of lamination quality after slots were machined.

After machining the stator slots laminations were visually inspected as shown in **Fig. A12.2(b).** There was no shorting observed in the lamination and Mylar windings. The electrical resistance across the layers was monitored and found to be high, indicating no shorting after the slots were machined.

Once the stators were machined they were tested on the Flux Dynamics motor stand, **Fig. A12.3(a)**. The setup includes a Baldor drive motor coupled to a Himmelstein torque meter on the rotor shaft. Testing consists of measurements at 600, 1200, 1800, 2400, 3000 and 4000 rpm. The gap spacing between the rotor and stator was set to 1 mm.

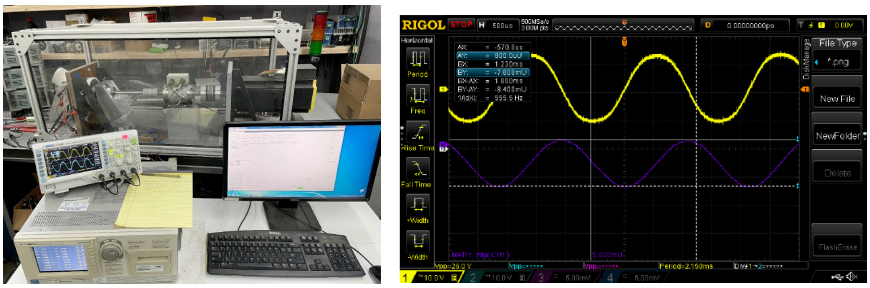

(a) (b)

Fig. A12.3. (a) Motor test stand; (b) Back EMF waveform for the FeCo stator.

A plastic stator was built to run a test stand for a baseline of frictional losses. These losses were subtracted out of final measurements to extract the stator losses. The back EMF waveform is shown in **Fig. A12.3(b)** for the FeCo stator. A similar waveform was also run for the FeNi stator and driven to saturation. The losses were calculated for the stators as a function of motor speed (**Fig. A12.4).** The FeNi stator exhibited approximately half of the losses of the FeCo stator. It is notable that these losses are very low and on the same order of magnitude as frictional losses. It is also found that the losses were mainly linearly increasing with speed suggesting losses driven by hysteretic rather than eddy current losses.

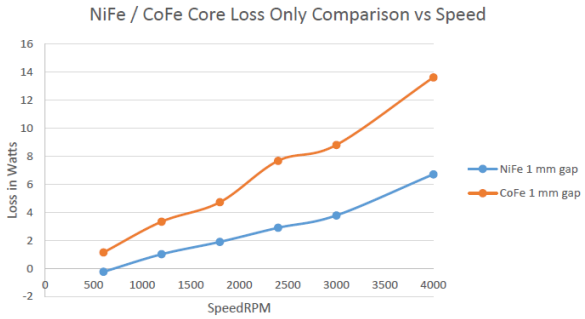

Fig. A12.4. Measured losses in the FeNi and FeCo stators.

In summary, Metglas was able to demonstrate castability of the CMU FeNi alloy with a high degree of confidence in moving to commercial production. A novel process was found to fabricate stators from the material. Losses were measured at a third party test location. The FeNi based stator showed losses nearly half of more conventional FeCo amorphous cores.